Turun yliopisto
University of Turku

THE ROLE OF DOPANT MORPHOLOGY IN SUPERCONDUCTING $YBa_2Cu_3O_{7-\delta}$ THIN FILMS

Mika Malmivirta

TURUN YLIOPISTON JULKAISUJA - ANNALES UNIVERSITATIS TURKUENSIS
Sarja - ser. AI osa - tom. 568 | Astronomica - Chemica - Physica - Mathematica | Turku 2017

Turun yliopisto
University of Turku

THE ROLE OF DOPANT MORPHOLOGY IN SUPERCONDUCTING $YBa_2Cu_3O_{7-\delta}$ THIN FILMS

Mika Malmivirta

TURUN YLIOPISTON JULKAISUJA – ANNALES UNIVERSITATIS TURKUENSIS
Sarja - ser. A I osa - tom. 568 | Astronomica - Chemica - Physica - Mathematica | Turku 2017

University of Turku

Faculty of Mathematics and Natural Sciences
Department of Physics and Astronomy
Wihuri Physical Laboratory

Supervised by

Prof. Petriina Paturi
Wihuri Physical Laboratory
Dept. of Physics and Astronomy
University of Turku
Turku, Finland

Dr. Hannu Huhtinen
Wihuri Physical Laboratory
Dept. of Physics and Astronomy
University of Turku
Turku, Finland

Reviewed by

Prof. Satoshi Awaji
Institute for Materials Research
Tohoku University
Sendai, Japan

Assoc. Prof. Nick Long
Robinson Research Institute
Victoria University of Wellington
Lower Hutt, New Zealand

Opponent

Dr. Jens Hänisch
Institute for Technical Physics
Karlsruhe Institute of Technology
Karlsruhe, Germany

ISBN 978-951-29-7011-7 (PRINT)
ISBN 978-951-29-7012-4 (PDF)
ISSN 0082-7002 (PRINT)
ISSN 2343-3175 (PDF)
Painosalama Oy - Turku, Finland 2017

Preface

Acknowledgments

This work was carried out in the Wihuri Physical Laboratory, Department of Physics and Astronomy, University of Turku, Finland. Jenny and Antti Wihuri Foundation, Finnish Cultural Foundation, Finnish Foundation for Technology Promotion and the University of Turku Graduate School's Doctoral Program in Physical and Chemical Sciences are acknowledged for their financial support.

It is a great honour to have Dr. Jens Hänisch as an opponent. I would like to express my gratitude to professor Satoshi Awaji and associate professor Nick Long for reviewing my thesis. I am grateful to Prof. Petriina Paturi for giving me the opportunity to pursue a PhD in the group of Magnetism and Superconductivity. Her experienced advice and guidance have been invaluable and made my thesis possible. I deeply appreciate the support along with inspiring and dedicated discussions with Dr. Hannu Huhtinen. Furthermore, the help of Dr. Teemu Hynninen has been vital for the simulation work.

Without my colleagues, former and present, this project would have been much more difficult. Especially Dr. Heikki Palonen has taught me a great deal and patiently answered the questions of a novice. Dr. Minnamari Saloaro has supported me and given practical advice on many things. I am grateful for sharing a room with Dr. Jussi Tikkanen for several years, your tips and tricks have made my life a lot easier! It has also been important for me to meet all people at Wihuri. Without you, my years for the thesis would have been much more burdensome.

During the thesis work, I have also had the opportunity to collaborate with people around the world and all the collaborations have taught me much. Prof. Sebastiaan van Dijken and Dr. Lide Yao and Mr. Sampo Inkinen, you did great work for my papers. Also, I am grateful to Mr. Hannes Rijckaert for taking excellent TEM images.

I consider myself lucky for having many friends for taking me away from work every now and then. It has been vital for the success of this entire project. Also, the support of my family has been most important, without you I would not have reached this far. Finally, thank you Kati for going side by side, caring and supporting me.

Turku, October 2017

Mika Malmivirta

Abstract

In this work, the effect of $BaCeO_3$ (BCO) and $BaZrO_3$ (BZO) dopants on structural and superconducting properties of $YBa_2Cu_3O_{7-\delta}$ (YBCO) superconducting thin films was studied. The main focus was in the flux pinning properties of the doped thin films but also changes in the intrinsic properties were measured. This thesis is based on experimental work but also a molecular dynamics simulation was written to model the angular dependence of critical current, $J_c(\theta)$.

The YBCO films were grown on $SrTiO_3$ single crystal substrates using pulsed laser deposition (PLD). The structural properties of the samples were studied using X-ray diffraction and transmission electron microscopy. Superconducting properties were studied using magnetic and transport measurements.

As deposited using PLD, BCO creates small particles with concentration-dependent diameter of some nanometres. BZO, in contrast, creates columnar defects parallel to YBCO c axis with concentration-independent diameter being in the range 5–10 nm. Both dopants affect the structure of YBCO although, due to the shape and larger interface area of the BCO particles, BCO creates much larger stress in the YBCO matrix.

The enhancements in J_c are most notable in BZO doped samples as the magnetic field is parallel to them. The angular dependence of BCO doped YBCO, on the other hand, is not much affected by the dopant. However, a clear decrease of the anisotropy parameter γ is seen. It is triggered by the change of the coherence lengths due to impurity scattering of electrons.

In contrast to BCO, BZO causes pronounced changes in the angular dependence. As the magnetic field is parallel to the rods, a wide peak in $J_c(\theta)$ (c peak) can be seen in an optimal sample. However, if the rods are short or splayed enough, no c peak is seen. The rod morphology can be controlled in many ways, for example the deposition temperature determines whether the columns are splayed or straight and continuous or not. Similar disappearance of the c peak was also seen in multilayer films with BCO and BZO doped layers if the BZO columns were short enough. The disappearance of the c peak was also modelled in a molecular dynamics simulation capable of anisotropic scaling. It can be explained using the vortex path model.

Tiivistelmä

Tässä työssä tutkittiin $BaCeO_3$ (BCO) and $BaZrO_3$ (BZO) lisäyksen vaikutusta $YBa_2Cu_3O_{7-\delta}$ (YBCO) suprajohdeohutkalvon rakenteellisiin ja suprajohtavuusominaisuuksiin. Päähuomio oli vuon lukkiutumisominaisuuksissa mutta myös sisäisiä ominaisuuksia mitattiin. Tämä väitöskirja perustuu kokeelliseen työhön, mutta sisältää myös molekyylidynamiikkasimulaation, jolla mallinnetaan kriittisen virran kulmariippuvuutta, $J_c(\theta)$.

YBCO-ohutkalvot kasvatettiin $SrTiO_3$ yksittäiskiteiselle kasvatusalustalle käyttäen laserhöyrystystä. Rakenteellisia ominaisuuksia tutkittiin röntgendiffraktiolla ja läpivalaisuelektronimikroskopialla. Suprajohtavuuusominaisuuksia tutkittiin sekä magneettisilla että virtamittauksilla.

Laserhöyrystyksellä kasvatettaessa BCO luo pieniä, muutaman nanometrin halkaisijaltaan, olevia partikkeleita, joiden koko riippuu BCO:n konsentraatiosta. BZO puolestaan luo kolumnaarisia kidevirheitä, jotka ovat yhdensuuntaisia YBCO:n *c*-akselin kanssa. Niiden halkaisija on 5–10 nm, ja se ei riipu konsentraatiosta. Kummatkin lisäykset vaikuttavat YBCO:n rakenteeseen, mutta muotonsa ja suuremman rajapinnan alan vuoksi BCO luo huomattavasti suuremman jännityksen YBCO-matriisiin.

Parannus J_c:ssä on suurin, kun magneettikenttä on BZO-kolumnien suuntainen. BCO-lisätyn YBCO:n kriittisen virran kulmariippuvuus ei taas toisaalta lisäyksestä huomattavasti muutu. Anisotropiaparametrissä γ nähdään kuitenkin selkeä lasku BCO:ta sisältävissä ohutkalvoissa. Sen aiheuttaa koherenssipituuksien muuttuminen elektronien epäpuhtaussironnan vuoksi.

Toisin kuin BCO, BZO aiheuttaa selkeitä muutoksia kriittisen virran kulmariippuvuuteen. Kun magneettikenttä on kolumnien suuntainen, optimaalisessa näytteessä nähdään leveä piikki $J_c(\theta)$:ssa (*c*-piikki). Kuitenkin jos kolumnit ovat liian lyhyitä tai hajallaan, piikkiä ei nähdä. Kolumnien muotoa voidaan kontrolloida monella tavalla. Esimerkiksi kasvatuslämpötila määrittää kolumnien suoruuden ja katkonaisuuden. Vastaava *c*-piikin häviäminen nähtiin myös monikerrosrakenteissa, joissa oli BCO- ja BZO-lisättyjä YBCO-kerroksia. Piikki hävisi, mikäli kolumnit olivat riittävän lyhyitä. Sama tulos mallinnettiin kriittisen virran anisotropiaskaalaukseen kykenevällä molekyylidynamiikkasimulaatiolla. Havaittu *c*-piikin häviäminen voidaan selittää vortex path -mallilla.

Articles included in this thesis

This thesis is based on the experimental work carried out at the Wihuri Physical Laboratory, Department of Physics and Astronomy, University of Turku during the years 2012 – 2017. The thesis consists of an introductory part and of the following publications:

[**P1**] M. Malmivirta, L. Yao, H. Huhtinen, H. Palonen, S. van Dijken and P. Paturi. Three ranges of $J_c(\theta)$ of $BaZrO_3$ doped $YBa_2Cu_3O_{7-\delta}$ thin films grown at different temperatures. *Thin Solid Films*, **562**, 554, 2014.

[**P2**] M. Malmivirta, H. Palonen, H. Huhtinen and P. Paturi. The dependence of resistively measured B_{c2} and B_{irr} on $BaZrO_3$ concentration in $YBa_2Cu_3O_{6+x}$ thin films. *Journal of Physics: Conference Series*, **507**, 012030, 2014.

[**P3**] M. Malmivirta, L.D. Yao, S. Inkinen, H. Huhtinen, H. Palonen, R. Jha, V. P. S. Awana, S. van Dijken and P. Paturi. The angular dependence of critical current of $BaCeO_3$ doped $YBa_2Cu_3O_{6+x}$ thin films. *IEEE Transactions on Applied Superconductivity*, **25**, 6603305, 2015.

[**P4**] M. Malmivirta, H. Palonen, S. Inkinen, L.D. Yao, J. Tikkanen, H. Huhtinen, R. Jha, V. P. S. Awana, S. van Dijken and P. Paturi. Dirty limit scattering behind the decreased anisotropy of doped $YBa_2Cu_3O_{7-\delta}$ thin films. *Journal of Physics: Condensed Matter*, **28**, 175702, 2016.

[**P5**] M. Malmivirta, H. Rijckaert, V. Paasonen, H. Huhtinen, T. Hynninen, R. Jha, V. P. S. Awana, I. Van Driessche and P. Paturi. Enhanced flux pinning in YBCO multilayer films with BCO nanodots and segmented BZO nanorods. *Scientific Reports*, **7**, 14682, 2017.

Articles relevant to this work but not included in this thesis

[**P6**] H. Huhtinen, H. Palonen, M. Malmivirta and P. Paturi. The effect of $BaCeO_3$ dopant concentration on magnetically obtained B_{irr} and B_{c2} in YBCO thin films deposited on $SrTiO_3$ substrates. *Journal of Physics: Conference Series*, **507**, 012020, 2014.

[**P7**] P. Paturi, M. Malmivirta, H. Palonen and H. Huhtinen. The effect of BZO dopant concentration on magnetically obtained B_{irr} and B_{c2} in YBCO thin films deposited on STO substrates. *Journal of Physics: Conference Series*, **507**, 012040, 2014.

[**P8**] H. Huhtinen, H. Palonen, M. Malmivirta, R. Jha, V. P. S. Awana and P. Paturi. Magnetically defined B_{irr} and B_{c2} in $BaCeO_3$-doped $YBa_2Cu_3O_{6+x}$ thin films grown under tensile and compressive strain. *IEEE Transactions on Applied Superconductivity*, **25**, 6605405, 2015.

[**P9**] P. Paturi, M. Malmivirta, H. Palonen and H. Huhtinen. Dopant diameter dependence of $J_c(B)$ in doped YBCO films. *IEEE Transactions on Applied Superconductivity*, **26**, 8000705, 2016.

[**P10**] M. Malmivirta, H. Huhtinen, Y. Zhao, J.-C. Grivel and P. Paturi. Thickness dependent properties of YBCO films grown on CLO/GZO buffered NiW substrates. *Journal of Low Temperature Physics*, **186**, 74–83, 2016.

[**P11**] M. Malmivirta, J. Jyrinki, H. Huhtinen, A. V. Pan, S. Rubanov, R. Jha, V. P. S. Awana and P. Paturi. A Structural Optimization of Ferrite/YBCO bilayers. *IEEE Transactions on Applied Superconductivity*, **27**, 8000705, 2017.

[**P12**] H. Huhtinen, J. Ulriksson, M. Malmivirta, J. Järvinen, R. Jha, V. P. S. Awana, S. Vasiliev and P. Paturi. Deposition of YBCO thin films in view of microwave applications. *IEEE Transactions on Applied Superconductivity*, **27**, 7501205, 2017.

[**P13**] M. Z. Khan, Y. Zhao, X. Wu, M. Malmivirta, H. Huhtinen and P. Paturi. Improved interface growth and enhanced flux pinning in YBCO films deposited on an advanced IBAD-MgO based template. *Physica C*, **submitted**, 2017.

Contents

1 Introduction

1.1 Motivation

Superconductivity was found over a hundred years ago. During the years, many discoveries have been made in the field, several of them being honoured with a Nobel prize. This shows that superconductivity is a versatile, important and challenging research topic. It is not only zero resistance at low temperatures but it is also the same current in much smaller wires which means a very high current density. Even when the cooling system is taken into account, the wire cross section is remarkably smaller than that of conventional copper wires with the same capacity.

Nowadays superconductors are used routinely in many areas [1, 2]. Probably one of the best known application is magnetic resonance imaging (MRI) systems, with superconducting magnets. Strong superconducting magnets are also used in accelerator physics and fusion reactors but also in levitating trains. Last but not least, the research usage of superconducting magnets allows to have strong and stable magnetic fields that would not be possible with conventional electromagnets. Other, emerging technologies are for example superconducting power grids, high voltage fault current limiters and stronger and more compact motors and generators. Using superconductors in high power applications could decrease the energy need remarkably because large industrial motors use a vast amount of electricity [3]. Additionally, superconductors can be used in low-power applications to make for example sensitive electronic filters [4].

Many commercial superconductors, like the ones used in MRI systems, require liquid helium for cooling. Nowadays helium is more and more expensive and thus developing solutions that work at the temperature of liquid nitrogen, 77 K, is of vital importance. A lot of work has been done to improve the properties of the high temperature superconductor $YBa_2Cu_3O_{7-\delta}$ (YBCO) [5], although the exact mechanism of superconductivity in YBCO is still not known. However, YBCO is not yet the mainstream choice for MRI magnets.

YBCO is a brittle and ceramic material and due to manufacturing issues, NbTi and Nb_3Sn are more conventionally used in superconducting magnets. Because of the brittleness and complex structure of YBCO, it is used in wires as a thin film, with a maximum thickness of only some micrometres. Making a bendable wire of YBCO is not a straightforward task and it has been vastly studied. Another optimization issue is to improve so-called flux pinning in wires. Magnetic flux penetrates YBCO as small bundles, vortices. Keeping the vortices still under higher magnetic field, current and temperature

is important because moving vortices cause energy dissipation. This dissipation can in the worst case lead to conductor heating which breaks the superconductivity. Additionally, due to the nature of pinning, the flux pinning engineering is best done separately for different applications.

Most typically, small non-superconducting areas are created into YBCO matrix to keep the vortices at their places. However, further increased understanding and additionally improved techniques are needed before YBCO will be more involved in our everyday life. The only reasonable way towards this aim is to do the optimization through increased understanding. In this thesis, flux pinning in YBCO thin films is studied using $BaZrO_3$ and $BaCeO_3$ nanosized non-superconducting inclusions, referred as dopants from here on. Their effect on various superconducting and structural properties is studied and the superconducting system is also modelled.

1.2 Basic properties of superconductivity

Probably the best known property of superconductors is the ability to carry electric current without any resistance at temperatures below critical value, T_c. This has been verified by measuring a current in a superconducting loop and after a long time no practical degradation was observed [6]. Superconductors also exclude magnetic field inside them and this effect is known as the Meissner effect. It means that superconductors are perfect diamagnets, with susceptibility of -1.

The current is carried by paired electrons that do not scatter from impurities. The electrons are paired at the Fermi surface and thus there is a gap in the density of states at the Fermi surface. This has also implications for example on heat capacity which has a discontinuity at T_c.

Superconductivity was first discovered in Hg, but also many other pure metals, like Nb, exhibit superconductivity at low enough temperatures. In some materials superconductivity emerges only at high pressures, like in Y or Bi. Superconductivity can also be found in more complicated systems with strong electron-electron correlation. Typically many of those materials are sensitive to hole or electron doping [7, 8] and as it is close enough to optimal, they become superconducting at oxygen doping dependent T_c. The first complex oxide superconductor was found in the family of copper oxide superconductors, $Ba_xLa_{5-x}Cu_5O_{5(3-y)}$ [9] at 1986. Later, superconductivity has been found also for example in FeAs compounds [10]. Recently, one of the highest T_cs has been measured on hydrogen sulfide under high pressure [11].

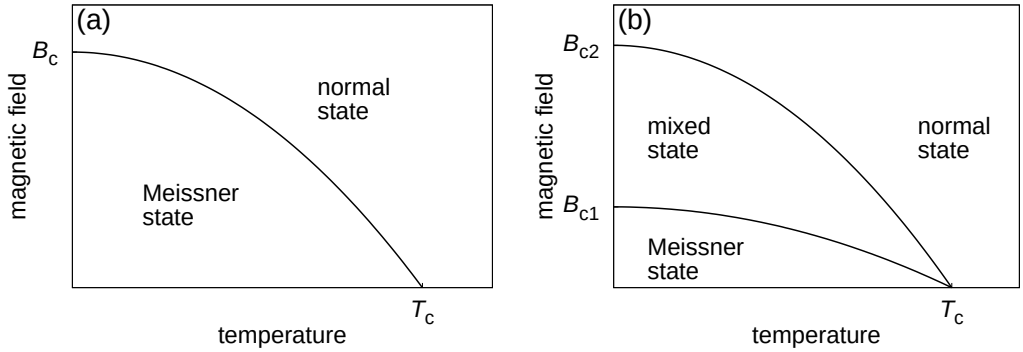

Figure 1. Phase diagrams for (a) type I and (b) type II superconductors.

Superconductors are classified in several ways, for example according to their transition temperature into high-temperature superconductors (HTS) and low-temperature superconductors (LTS). The limit between HTS and LTS is usually taken to be around 30 K. However, the classification based on the critical temperature is misleading since HTS usually refers to superconductors which cannot be described using the conventional microscopic quantum theory. Alternatively, superconductors can be divided into type I and type II according to their behaviour in magnetic field, B. Type I superconductor expels magnetic field as long as it is smaller than the critical value. This is the so-called Meissner state. At higher fields, superconductivity breaks down and superconductor returns to the normal state. The critical value of field depends on temperature, as can be seen on the phase diagram of type I superconductor in figure 1 (a). Type I superconductors are mainly pure elements and the values of the critical fields are clearly below 1 T even at 0 K [12, p. 261].

On the contrary, type II superconductors have two critical fields (figure 1 (b)). At $B < B_{c1}$ the superconductor behaves as type I in the Meissner state but at intermediate fields $B_{c1} < B < B_{c2}$ in the mixed state, magnetic field penetrates the superconductor as small bundles, vortices. The flux through one vortex is always a flux quantum, $\phi_0 = \frac{h}{2e}$, where h is Planck constant and e the electron charge. At fields higher than B_{c2} the superconductivity breaks down. The B_{c2} is much higher than the critical field in type I and this makes type II much more important group from the applications point of view.

The classification into type I and II can also be made quantitatively using characteristic parameters, the magnetic penetration depth, λ, and the coherence length, ξ. The magnetic penetration length describes the decrease of the magnetic field at the superconductor-normal interface and the density of superelectrons can change in the

length order of ξ. The ratio $\kappa = \lambda/\xi$ is used to precisely define the difference between type I and type II. If $\kappa > 1/\sqrt{2}$, superconductor is type II, otherwise type I. In most cases of interest $\kappa \gg 1/\sqrt{2}$, i.e. $\lambda \gg \xi$, which causes the sum of positive magnetic energy and negative electron condensation energy to be negative at the superconducting/normal interface. Thus it is favourable for the type II to create boundaries between normal and superconducting state by allowing the magnetic field to penetrate the superconductor and create non-superconducting areas.

The coherence length can also be thought as a measure of distance over which one electron can affect the state of other current carriers. This interaction and thus the coherence length can be restricted by impurities. In the so-called dirty limit the coherence length is restricted by the mean free path of electrons as [13, p. 410]

$$\xi_{\mathrm{i}}^{-1} = \xi_0^{-1} + l^{-1}, \tag{1}$$

where ξ_{i}^{-1} is the impurity-restricted coherence length, ξ_0^{-1} the unrestricted coherence length and l the mean free path of the current carrying electrons.

The existence limits of superconductivity depends, above all, on material. For a certain material the existence of the superconducting phase is determined by a combination of temperature, magnetic field and current. For instance, the lower is the temperature, the higher currents the superconductor can withstand without breaking into normal state. Similar trend is with magnetic field, as can be seen in figure 1. Modifying the existence limits of superconductivity is one of the key targets of the current superconductor research. Studies are mostly focused on aiming at higher critical currents.

Although superconductivity has been studied for over a hundred years, the phenomenon is still not fully understood. The BCS theory [14] (after its inventors, Bardeen, Cooper and Schrieffer) was published in 1957. The theory explains superconductivity in LTS materials but fails in all HTS materials. Already before that, a model describing type I superconductors phenomenologically, had been presented by Ginzburg and Landau [15] (later, GL theory). Although meant for type I superconductors, the GL equations have been used to describe also HTS materials.

1.3 Flux pinning

Vortices are affected by many forces. A vortex is repelled by other vortices. Additionally, in the presence of electrical current, vortices experience Lorentz force which tries to move them. This happens already without transport current since the expelling of magnetic field is done by creating screening currents in the superconductor. The

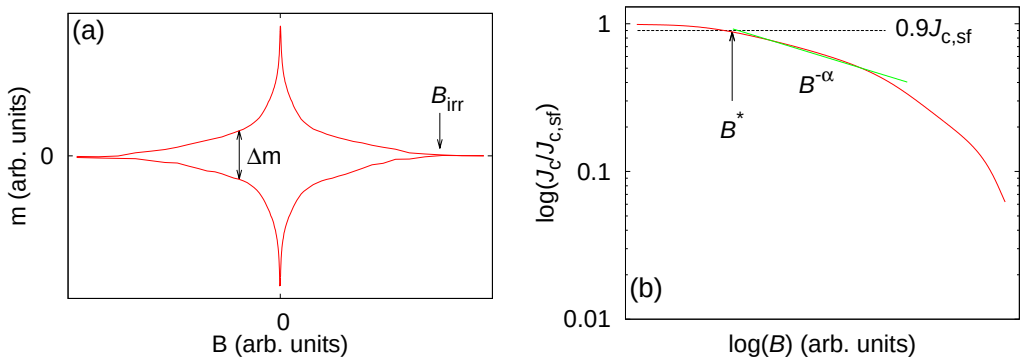

Figure 2. (a) Schematic diagram of the magnetization of a superconductor as a function of external magnetic field. (b) The J_c extracted from the magnetization loop, scaled with the self-field J_c, $J_{c,sf}$.

unbalanced forces cause movement of vortices which results in energy dissipation and hence resistance. Thus, preventing the vortex movement is crucial. Vortices lower their energy by going into non-superconducting areas, into so-called pinning centres, where the superelectron density is suppressed. It is energetically favourable for vortices to be in a pinning centre instead of breaking the superconductivity. Naturally vortices tend to form a hexagonal vortex lattice. With a higher field, this order is disturbed and finally at even higher fields they start to move, forming a vortex liquid [16].

The pinning capability of a pinning centre is determined e.g. by the size and shape but also the distribution of the particular defect [17]. The defects can be either intrinsically present in the material or they can be artificially introduced. The optimal size of a pinning centre in the perpendicular direction of the vortex is 2ξ. In the optimal case there is one vortex for each pinning site, which yields the optimal density of $B/\phi_0 \approx B/2 \cdot 10^{11}$ cm^{-2}, where B is the magnetic field in tesla. The coherence length ξ is temperature dependent but it is also a material specific parameter.

By affecting pinning properties, the current carrying capability can be enhanced. The critical current density, J_c, is defined as the highest current density that a superconductor can stand maintaining the resistanceless current flow. By using artificial pinning centres one can also modify the irreversibility field, B_{irr}, which is the field above which vortices start to move and thus resistance emerges. The J_c is often determined by measuring the sample magnetization as a function of the external magnetic field and in those measurements the loop closes at B_{irr}(figure 2 (a)). All the variables related to pinning like coherence length, critical current density and irreversibility field have temperature

dependence. Thus, the optimization of the pinning landscape is needed for every situation separately.

1.4 Models for critical current

The Bean critical state model is commonly used to determine the magnetic field dependence of the J_c using easily measurable sample magnetization. The model assumes that the screening current is at the critical limit, where present. For thin films in the case of magnetic field perpendicular to the plane of the film, the J_c can be calculated as [18]

$$J_c = \frac{2\Delta m}{d_x[1-\frac{d_x}{3d_y}]V}, \tag{2}$$

where d_x and d_y are the edge lengths of the thin film ($d_y \geq d_x$) and V is the volume of the sample and Δm the opening of the magnetization hysteresis loop (figure 2 (a)). The model has been widely used because of the ease of use and accuracy. However, care has to be taken when comparing the obtained J_c values with values attained using different methods [19].

The magnetic field dependence of J_c is an important parameter from the applicability point of view. The decay of J_c in magnetic field is conventionally characterized by fitting a function $J_c \propto B^{-\alpha}$ above the so-called accommodation field, B^*. Accommodation field is the point at which the vortex-vortex interactions start to dominate instead of single vortex pinning. The common definition for B^* is $J_c(B^*) = 0.9J_c(B=0)$ [20, 21]. This definition has been used in [**P1**] and [**P3**]. A schematic example of the accommodation field along with the exponent α fit is shown in figure 2 (b). Typically, α values ≈ 0.5 are observed with small pinning sites, such as dislocations [22]. In samples with large defects, α typically decreases down to ≈ 0.2. This is caused by the breaking of the vortex lattice by the large pinning sites. The model assumes that the decay of J_c follows power law but this is, however, not always true. For example samples with columnar pinning sites exhibit more round behaviour as J_c is expressed in double logarithmic scale [23]. Thus fitting α in such case does not give consistent results and the fitting result is best used as a suggestive parameter. Thus more complicated models have been developed (e.g. in [22]), taking better into account the different shapes of the $J_c(B)$ curves. Fitting those models is however, rather complicated and thus the simple model can serve as a rough estimation in most cases.

In addition to the magnetic field dependence of J_c, the angular dependence of J_c in a constant magnetic field is an important feature. Many type II superconductors are naturally anisotropic, which means that some of their characteristic parameters change as the

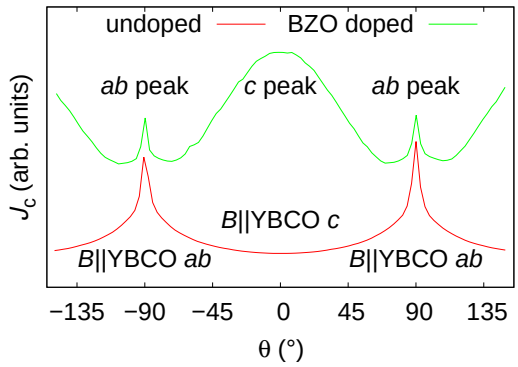

Figure 3. Typical angular dependence of the critical current of an undoped and BZO doped YBCO sample. In addition to a intrinsic peak at $\pm 90^\circ$, a peak due to correlated defects at 0° can be seen in the BZO doped sample.

direction of the magnetic field is changed with respect to the lattice. The anisotropy has been described by Blatter [16] using the electron mass anisotropy parameter, $\gamma^2 = M/m$, where M is the effective electron mass in the c direction and m in the ab direction. Typically for YBCO γ is in the range 5–7 [16, 24, 25]. The anisotropy ratio is used in the scaling function

$$\varepsilon_\vartheta^2(\theta) = \frac{\sin^2\theta}{\gamma^2} + \cos^2\theta, \tag{3}$$

where θ is the angle between the external magnetic field and the axis along which M is defined. This equation can be used to scale the anisotropic properties into isotropic by applying it to relevant variables. For example, this equation is used in [**P4**] to determine the anisotropy parameter from the angular dependence of B_{c2}. However, because J_c depends also on extrinsic flux pinning properties, equation (3) cannot be directly applied to it.

Anisotropy of a type II superconductor is also reflected into the shape of the critical current density, $J_c(\theta)$. As an example, a $J_c(\theta)$ of an undoped YBCO thin film sample is shown with a red line in figure 3. The curve shows a characteristic peak as $B||ab$ plane of YBCO (labelled as *ab* peak). If the sample additionally contains correlated defects parallel to YBCO c axis, a peak can also be seen as the field is parallel to them, as can be observed from the green curve in figure 3 (labelled as *c* peak). The $J_c(\theta)$ can be modelled using the vortex path model [26–29]. It can also been used to identify different defects in a superconductor, as proposed by Knibbe *et al.* [30]. A single vortex minimizes its energy by being at optimal pinning sites. As averaged over many vortices

and steps, the formation of $J_c(\theta)$ can be seen as a statistical process. In the model, vortices follow pinning sites that are parallel to the thin film plane or perpendicular to that.

In the model, the total critical current density is composed of three parts [28]

$$J_{c,tot}(\theta) = J_c(\theta) + J_c(\theta + 90^\circ) + J_{c,rand}(\theta). \tag{4}$$

In the equation (4) above,

$$J_c(\theta) = J_0 \left[\frac{1-\eta}{\sin^2(\theta)} \exp\left(-\frac{1}{2\Gamma_G^2 \tan^2(\theta)} \right) + \frac{\eta}{\cos^2(\theta) + \Gamma_L^2 \sin^2(\theta)} \right], \tag{5}$$

where η is the mixing parameter of the peak and Γ_L and Γ_G are parameters giving the width of the Lorentzian and Gaussian peak shape and J_0 is a scaling constant. The intrinsic *ab* peak at $\theta = \pm 90^\circ$ is fully Lorentzian ($\eta = 1$). For the *c* peak at $\theta = 0^\circ$, the equation (5) is shifted by 90° and a pseudo-Voigt distribution is used ($\eta \leq 1$). The random part, $J_{c,rand}(\theta)$ is a constant, $J_{c,0}$, scaled using equation (3), like $J_{c,0}/\varepsilon_\vartheta(\theta)$. The practical realization of the vortex path model used in this thesis follows the procedure presented in [28].

The fitting parameters can be used to calculate the full width at half maximum (FWHM) values of the fitted peaks. Since there are many free parameters, great care has to be taken that the fitting procedure is done consistently. Using the Pseudo-Voigt distribution, the FWHM can be approximated as $2(1-\eta)\exp(\Gamma_L^2/\Gamma_G^2) + \eta\Gamma_L$. Furthermore, if $\Gamma_{L,G} < 1$, a peak in $J_c(\theta)$ can be seen. If $\Gamma_{L,G} > 1$, the vortex step length along the columnar pinning sites is shorter than the standard deviation of the sideways steps and no peak is seen. In this case, for the Lorentzian peak shape the peak will shift 90° in position and for the Gaussian shape, local maxima can appear as shoulders around the *ab* peak [28]. In the original vortex path model [27], $J_c(\theta)$ is described for both Gaussian and Lorentzian peak shape but the pure forms do not describe single films at all temperatures and fields well enough. Therefore, the more complicated Pseudo-Voigt distribution was used in [28] and in this work.

1.5 $YBa_2Cu_3O_{7-\delta}$

The high-temperature superconductor $YBa_2Cu_3O_{7-\delta}$ (YBCO) was found in 1987 [31]. Nowadays it is studied due to its high current carrying capability and high critical fields, even at the temperature of liquid nitrogen, 77 K. It belongs to the cuprate family where the supercurrent is carried by the CuO_2 planes. YBCO is superior to conventionally

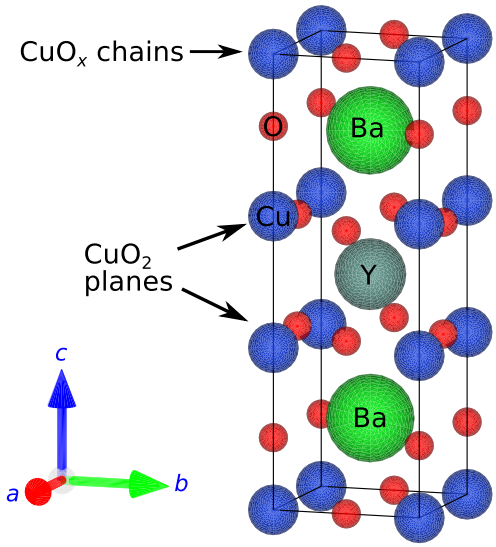

Figure 4. The structure of YBCO in orthorhombic phase. Data taken from [33], drawn using VESTA [34].

used NbTi and Nb_3Sn in many quantities [32]. However, due to complex production issues [17], there is still optimization work to be done.

As a superconductor, YBCO is orthorhombic (figure 4), with unit cell parameters $a = 3.82$ Å, $b = 3.89$ Å and $c = 11.68$ Å [33]. In the structure, Y atom (grey in the figure 4) is in the middle, Ba atoms (green) in above and below that. Copper atoms (blue) are located in b axis and on CuO_2 planes, oxygens being red. The CuO_x chains along the b axis and the BaO planes serve as a charge reservoir for the CuO_2 planes.

The structure of YBCO is sensitive to the oxygen content. When $\delta > 0.7$, YBCO is tetragonal and not superconducting [35]. By adding oxygen, the antiferromagnetic structure turns into being capable of superconductivity at $\delta < 0.7$ [35]. The oxygen goes into the CuO_x chains in the direction of the b axis [36]. With the optimal oxygen deficiency, around $\delta \approx 0.05$, the T_c can be as high as 94 K [35]. During YBCO thin film deposition, the transition from tetragonal into orthorhombic is done by adding oxygen into the chamber at high temperature. For example at 700 °C this transition occurs roughly at atmospheric pressure [36, 37].

YBCO is a high-κ superconductor, meaning that the $\lambda \gg \xi$. From the practical point of view, this implies that by tuning the flux pinning properties, its performance can be greatly affected. The coherence length of YBCO at 0 K in the ab plane, ξ_{ab}, is 1.6 nm and $\xi_c = 0.3$ nm [25], determined using magnetization measurements of single

crystals. The magnetic penetration depth in the *ab* plane, λ_{ab}, is 130 nm in the *c* direction 450 nm [24], determined also by measuring the magnetization of single crystals. However, variation in results exists in both ξ [38] and λ [24, 39] values although some variation can be accounted to differences in the measurement techniques.

1.6 Defects in YBCO

There are various different defects naturally present in YBCO thin films. For example point defects can be found, such as vacancies or interstitials. Dislocations are also common. They are formed for example when two slightly differently oriented areas accommodate their structures and usually use dislocations to relieve strain. Depending on the growth method, dislocations can be found for instance in YBCO thin films at the boundaries between growth islands [40].

Due to the transition from tetragonal to orthorhombic during the thin film deposition, twin boundaries are typical defects in YBCO. Twins are formed to relieve strain, caused by for example cubic substrates. Twins are areas where *a* and *b* axes are swapped, i.e. the crystal is mirrored along {110} planes. The length of the twin boundaries can be hundreds of nanometres, even more on thick films [41]. Furthermore, the twin structure can be affected by selecting deposition targets with either nano- or micron sized grains [42]. In YBCO, there can additionally be grain boundaries that are different from twin boundaries. In a grain boundary, grains with arbitrary difference in the in-plane directions of the crystal axis, meet. If the angle between grains is too large, it degrades current remarkably and this is especially an issue in films on technical substrates. Solving the grain boundary problem has required a lot of work on YBCO for applications [32]. Although there are no dislocations in twin boundaries but only in twin domain boundaries, the effect of twin boundaries on J_c is similar to grain boundaries below 2° [43].

Also stacking faults are commonly seen in the layered structure of YBCO. In a stacking fault the layer structure is disturbed. The stacking fault density can be affected by thin film deposition conditions [44, 45]. Furthermore, due to too low deposition temperature and thick films, also *a* axis upwards oriented grains are seen [46–48].

Superconductivity is suppressed in every defect, and the strength of the suppression defines the pinning capability of a defect. From the flux pinning point of view, the defects can be divided into non-correlated and correlated defects. Non-correlated defects have a random distribution and orientation. Correlated pinning defects consist of parallel linear and planar defects. Their effect on pinning is strongest when the magnetic

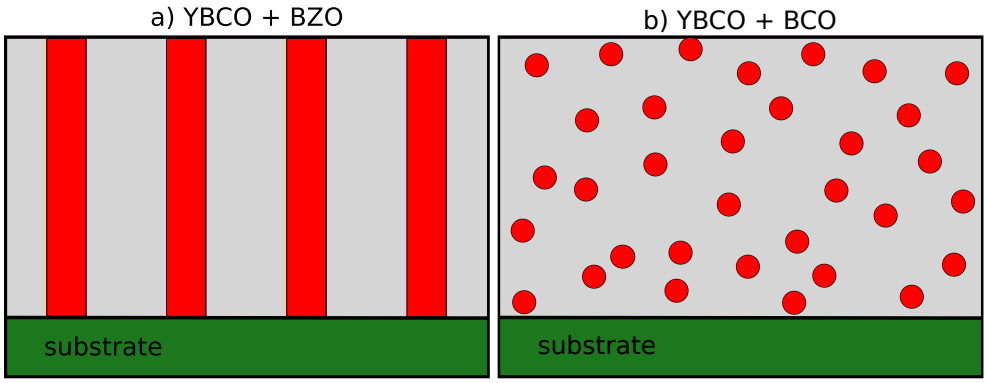

Figure 5. The schematic diagram of the (a) BZO and (b) BCO growth in YBCO matrix as grown by PLD.

field is parallel to them, or at least close to that. Furthermore, flux pinning can be divided into weak and strong pinning. As a simplification, all larger defects act as strong pinning sites and smaller defects are weak. A pinning site is strong if it is capable to pin a vortex by itself whereas weak pinning sites need collective effect of the defect structure to be able to pin a vortex [49]. For example twin boundaries are strong but individual point defects are weak.

To achieve even higher flux pinning forces, additional defects, using various techniques, have been introduced to YBCO thin films. One way is to mix non-superconducting dopant into the YBCO matrix and commonly many $BaMO_3$ compounds have been used, where M is metal, like Zr or Sn or Ce. The defects degrade the superconducting properties and reduce the superconducting volume. However, up to certain limit, many dopants increase J_c. There is an interplay between superconductivity and optimal type and density of defects.

Probably one of the most popular dopants is $BaZrO_3$ (BZO), which is a cubic perovskite with 4.19 Å lattice parameter [50] and thus the in-plane lattice mismatch with YBCO is approximately 9 %. One reason for using it as a dopant is that it does not react with YBCO [51]. BZO forms a correlated array of parallel, columnar defects [52–54] in the direction of YBCO c axis when grown by pulsed laser deposition (PLD). The rod diameter is roughly 5–10 nm but the density depends on the dopant concentration [21, 55], being 1300 μm^{-2} for 2.9 wt-% sample [56]. Furthermore, in some works it has been found that the rods are not entirely BZO but between BZO areas there is distorted YBCO [57]. Schematically the structure in YBCO matrix is shown in figure

5 (a). The rods grow cube-on-cube but at high dopant concentration, 9 wt.%, a small fraction of *a* axis grains are seen [21, 58]. The BZO rods pin most strongly when the magnetic field is parallel to them. Then, if the rods are continuous enough, usually a peak in $J_c(\theta)$ can be seen [59]. The optimal concentration depends on the magnitude of the magnetic field [58].

Also some other dopants create similar rod-like structures in YBCO matrix, like $BaSnO_3$ (BSO) [60, 61], having slightly larger rod diameter, around 10 nm but also $BaHfO_3$ [62], giving 5 nm rod diameter in $GdBa_2Cu_3O_{7-\delta}$. Additionally, rods have been created using Ba_2YNbO_6 [63] and those rods can be fine-tuned using Ba_2YTaO_6 [64].

YBCO has also been doped using non-correlated pinning centres, like $BaCeO_3$ (BCO), which is also an orthorhombic perovskite [65]. However, for simplicity in this thesis it is indexed as cubic with lattice parameter roughly 4.4 Å [66]. The lattice mismatch with YBCO *ab* plane is roughly 14%. Unilike BZO, BCO creates small particles, nanodots, with a diameter of a couple of nanometres [67],[**P3**]. Schematically the structure of BCO in YBCO is shown in figure 5 (b).

Another commonly used dopant is Y_2O_3, which forms nanodots [68]. On the other hand, usually nanodots are accompanied by BZO [69] or BSO nanorods [70]. Also other methods to create distortions in YBCO are used. For example Y substitution by Pr [71] and irradiation of samples [72]. However, neither of them has been as widely used as doping using non-superconducting material.

Doping, in general, adds strain into YBCO lattice and the growth depends on the dopant properties but is also sensitive to growth conditions. For example YBCO *c* axis lengthens, similarly than in oxygen deficient YBCO [35, 73]. Along with the increased strain, the T_c is also decreased, but usually only some kelvins at most. The J_c is, however, improved especially in magnetic fields due to increased amount of defects for pinning centres. The angular dependence of the critical current is also greatly affected. Effectively, dopants decrease the effective anisotropy, i.e. the maximum variation of the $J_c$values as sample is tilted in magnetic field. Intrinsically, there is a peak as the magnetic field B is parallel to the *ab* plane but a peak as $B||c$ axis of YBCO is an implication of correlated defects in the sample. Defects can also affect the intrinsic anisotropy parameter [74, 75], but also opposite results exist [45, 76].

1.7 YBCO growth

As deposited using PLD, YBCO typically forms growth islands [77]. Certain dopants, like BZO, form rods due to the strain between dopant and YBCO matrix [78], like InAs

islands on GaAs(100) [79]. Strain has been found to determine, whether dopant forms correlated or non-correlated structure [80]. However, the growth of the dopants also depends on the growth method. For example BZO forms rods when grown by PLD, but when grown by chemical solution deposition (CSD), BZO forms non-correlated, 50 nm sized particles [76, 81, 82]. Thus, due to different BZO morphology, no c axis peak is observed in the angular dependence of J_c.

The temperature of the substrate has also many effects on the growth of thin films. Too low deposition temperature, T_{dep}, can lead to nonstoichiometry as some of the material condenses and more volatile components evaporate before the next pulse hits the substrate. Furthermore, the diffusion length is smaller at low T_{dep} and thus defects are created more easily [83, p. 262–263]. Also, due to decreased mobility the YBCO growth island size is smaller [84]. For undoped YBCO, low substrate temperature is seen to lead to $YBa_2Cu_4O_x$ layers and higher temperature to Y-Cu-O nanocolumns [85]. This change has been attributed to Ba-Cu-O liquid phase during growth above certain T_{dep} and this change results in completely different structure of $J_c(\theta)$. Similar $J_c(\theta)$ characteristics are also seen in a study by Xu *et al.* [45] but they see no columnar defect structure at low T_{dep}. Their sample deposited at low T_{dep} has stacking faults and at high T_{dep} there are Y_2O_3 defects. On the contrary, in a study by Wang *et al.* [44] more stacking faults with higher T_{dep} were seen. On the other hand, too low T_{dep} can also cause degradation of YBCO crystal structure [52]. It can be concluded that there is no single phenomenon that could be straightforwardly controlled with the selection of T_{dep}.

The T_{dep} affects also on the growth of BZO. With higher substrate temperature during deposition, more ordered and longer columns can be achieved [69, 78]. Similar behaviour has also been modelled for YBCO with vapour phase epitaxy [86]. Due to changes in the pinning landscape, also changes in superconducting properties can be seen. For example, with high enough T_{dep}, the c axis peak emerges in $J_c(\theta)$ [69]. Also, clear improvements in $J_c(B)$ can be seen [87]. Furthermore, by rising T_{dep} the decrease in T_c can been compensated [87].

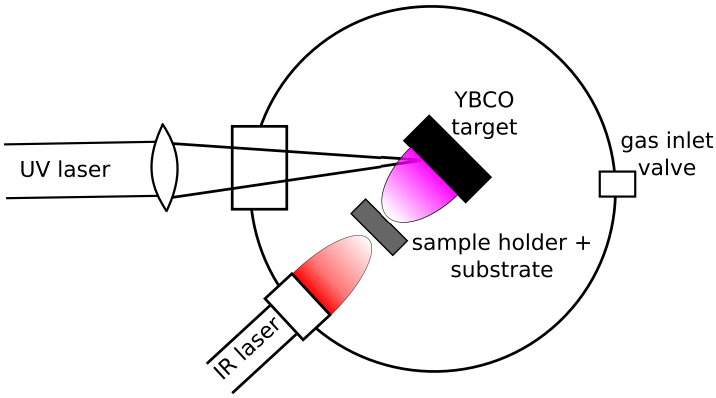

Figure 6. A schematic diagram of a pulsed laser deposition system.

2 Experimental

2.1 Pulsed laser deposition

Pulsed laser deposition (PLD) is a thin film growth method. High energy laser evaporates the solid substrate material which then condenses on the substrate. PLD is used to grow many complex oxide compounds due to good stoichiometric material transfer. However, due to its slow growth speed and difficulties in growing large areas, it is not common in commercial solutions. For YBCO, PLD is mainly used for research purposes, although some commercial PLD made YBCO wires also exists. Additionally, PLD reproduces the substrate structure well and for instance different substrates can be used to compare the effects of strain on samples. It can also be used to deposit samples on technical substrates, although to make a good films, the buffer layer on the technical substrate has to be carefully optimized [88]. As it was discussed in section 1.7, the growth of YBCO and dopants is highly dependent on selected method. Although the BZO rods produced by PLD are usually better for pinning, the CSD method can be for example much more easily scaled up.

In the thin film fabrication process in this work, the $SrTiO_3$ (STO) substrate is attached on an sample holder, an inconel plate, using silver paste. The temperature of the substrate is controlled via a thermocouple that is attached to the plate. The main part of the sample chamber (figure 6) is the substrate with holder and YBCO target. In the set-up used in this thesis for multilayer samples, up to four different targets can be deposited and targets changed *in-situ*. The UV laser for the material deposition comes in from an optical window, as well as the IR laser for heating the sample holder. The

chamber is pumped with a turbo pump backed with a scroll pump. There is also a valve to let the oxygen into the chamber.

The chamber is first pumped and some oxygen is let in to avoid the oxygen depletion from the substrate. During the heating process with 25 °C/min the pressure is set into 23 Pa in flowing oxygen. The deposition is done at 5 Hz frequency with an XeCl excimer laser (λ = 308 nm, fluence = 1.3 J/cm^2). The deposition temperature can vary, but for example in [**P5**] it was the most commonly used 750 °C. The correct deposition temperature is essential for the desired crystal quality. The oxygenation is usually done in lower temperature than deposition, often at 700 °C, like in [**P5**]. During the introduction of the oxygenation, and thus higher pressure, the phase transition from tetragonal into orthorombic phase occurs [37]. To avoid undesired effects, the transition from ablation to oxygenation was done in 10 °C/min whereas after 10 min of oxygenation, the sample was cooled 25 °C/min.

2.2 Atomic force microscopy

Atomic force microscopy (AFM) is a method than can be used to probe the topography of a surface. In contact mode the measurement probe touches the surface and works in the repulsion regime of a Lennard-Jones type potential. The force that probe presses the surface is kept constant and the position of the probe is varied accordingly. Commonly, the movement of the sample, both in the plane of the sample and height position, is done by using a piezo element. The position of the probe cantilever is monitored using a laser detector and this configuration allows sub-nm accuracy in the direction perpendicular to the surface plane.

In this thesis work AFM was used to measure the width and height of the current stripes for transport measurements. Film inequalities due to etching precipitates caused some variations into the measured heights but their effect was reduced by making several measurements for one sample. More generally, AFM can also be used to measure surface roughness and to see for example growth irregularities of samples. This can be useful especially when studying the growth of samples.

2.3 X-ray diffraction

X-ray diffraction (XRD) is a technique to determine the crystal structure of material. It utilizes the diffraction of X-rays from different parallel lattice plains. The X-ray wavelength range is between $10^{-12} - 10^{-7}$ m and commonly is used radiation from the copper K_α excitation with wavelength 1.54 Å. A diffraction maximum is seen at

the detector as the distance of the reflection of the X-rays from successive planes is a multiple of the wavelength and this is known as the Bragg's law.

In a conventional X-ray powder measurement peaks originating from all crystal directions are seen, although some of them are weaker or even vanish due to the type of the atoms in the base or due to the structure of the lattice. Thin films, however, do not have all crystal orientations. This means that to have a diffraction maximum, also the angular positioning of the sample has to be correct in order to see a diffraction peak whereas in powder samples only the angle between incoming and diffracted X-rays, 2θ, has to be correct. The ϕ angle is the rotation of the plane of the sample and ψ the tilt of the sample in the texture cradle. In this thesis, a Philips X'Pert Pro MPD with a Schulz texture goniometer was used. Soller slits 0.04 rad were used to filter out non-parallel X-rays and masks and slits to pass the beam properly cropped on the sample and finally to the detector. Furthermore, to cut out the peak due to Cu K_β radiation, a Ni filter was used.

All the thin film samples were similarly characterized. A $\theta - 2\theta$ scan was made to determine the lattice parameters and strain in the c axis of YBCO. The c parameter was determined from the YBCO (005) and (004) peaks. More than one peak was used to eliminate the zero-point error. The strain in the c direction was determined from the full width at half maximum (FWHM) value of the YBCO (005) peak. Even though there are other things, like instrument related broadening and size broadening, they are approximately constant in the system and thus comparing the widths of the peaks gives a reasonable measure of the strain in the lattice. The YBCO peaks were also used to roughly determine the oxygenation level of YBCO. The intensity ratios of YBCO peaks $I(005)/I(004)$ and $I(005)/I(007)$ depend on the oxygenation level [73]. Furthermore, the $\theta - 2\theta$ diffractogram was used to make sure that there are no impurity peaks. In addition to YBCO $(00l)$ peaks, there are STO substrate $(00l)$ peaks that overlap with YBCO (003), (006)... because YBCO $c \approx 3a_{\mathrm{STO}}$. Furthermore, the strongest substrate peaks are additionally seen as K_β peaks at smaller 2θ than the actual K_α peak. Also, there are peaks from the sample holder and possible dopant peaks.

By measuring the rocking curves of YBCO (005), the splay of the YBCO unit cell could be determined. The measurement was done by keeping the 2θ constant and varying the ω which is the angle between the sample and the X-ray source. Furthermore, together with the c parameter, it can be used to measure the correlation length in crystal [89].

Two-dimensional $2\theta - \phi$ scans were made on YBCO (102) and YBCO (212). The (102) peak was scanned in two different orientations, the YBCO a axis in-plane and out-of-plane, meaning different ψ angle. The FWHM of that peak in the ϕ direction also reflects the splay due to the grain boundaries in the sample and this measurement can also be used to confirm the texture of the samples, if the peaks are at the right place. The two-dimensional scan of YBCO (212) was used to determine twinning of the sample [42]. Biaxially twinned samples can be seen as four separate peaks: two at the same 2θ, different ϕ being YBCO (212). Respectively, there are two peaks of YBCO (122) with constant 2θ but different ϕ.

2.4 Transmission electron microscopy

Transmission electron microscopy (TEM) utilizes the wave nature of accelerated electrons to see the structure of material up to atomic scale. The electron beam is directed onto the sample area using electromagnetic lenses. The lenses are different coils and by adjusting them correctly, a desired electron beam can be attained. The electrons interact with the sample and some of them are absorbed and some transmitted. Behind the sample, there are lenses to focus the image on the detector.

TEM can also be used in various modes depending on the desired outcome. For example in scanning transmission electron microscope (STEM) mode the sample is scanned with the electron beam. It is also possible to obtain a diffraction pattern from small area of the sample to see the local crystal structure. Furthermore, the elements in the sample can be studied by energy-dispersive X-ray spectroscopy (EDX). In all the measurement modes the sample has to be thin enough so that the electrons can pass through.

The TEM imaging for the works included in this thesis were taken by staff at the Aalto University Nanomicroscopy Center (Aalto-NMC) for [**P1**], [**P3**] and [**P4**]. The TEM measurements for [**P5**] were made at the Ghent University, Department of Inorganic and Physical Chemistry. In both cases, a 200 kV JEOL 2200FS TEM was used. However, the sample preparation procedures were different. For [**P1**], [**P3**] and [**P4**] the wedging cross-sectional specimen were made by mechanical polishing method. First a structure Si/film/Si structure was glued and cut into thin slices. It was ground and polished by MultiPrep polishing (Allied High Tech Products Inc.) system and finalized using Ar ion polishing system (Model 691 PIPS, Gatan Inc.) For [**P5**] a cross-sectional lamella was made with a FEI Nova 600 Nanolab Dual Beam FIB-SEM using *in situ* lift

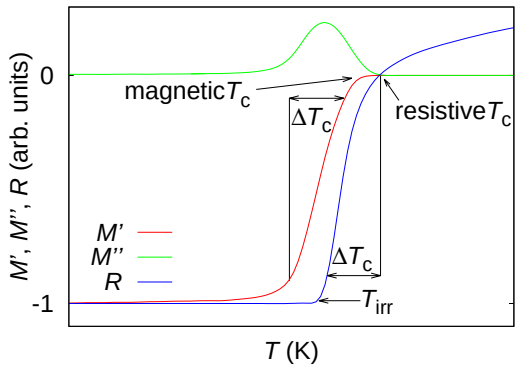

Figure 7. A schematic figure of the AC magnetization and resistance of a sample as a function of temperature. The determined transition temperatures and the widths of the transitions are also shown. The M' is the in-phase and M'' the out-of-phase magnetization, R the resistance of a sample.

out procedure with an Omniprobe extraction needle and top cleaning [90]. The analysis of the particle size in [**P3**] and [**P4**] was made using the ImageJ software.

2.5 Magnetic measurements

Magnetometers can be used to measure the magnetic moment of a sample inductively. It can be made either in DC- or AC-mode. In the DC-mode sample is vibrated inside the pick up coils and according to Lenz's law this induces into the coils a voltage proportional to the change of flux in the detection coils. The flux is proportional to the magnetic moment of the sample. In the AC-mode sample is not moving but a small drive AC-signal induces changes in the magnetic moment of the sample. The sample's response for that drive is recorded and that signal is proportional to the derivative $\mathrm{d}M/\mathrm{d}H$, where M is the magnetization of the sample and H the excitation field. Compared to DC, the AC-measurements are more sensitive to probe small changes in the magnetization.

Both the magnetic DC- and the AC-measurements in this work were made with the AC-measurement system (ACMS) of the Quantum Design Physical Property Measurement System (PPMS). The transition temperature was measured with an AC-magnetization scan with a 0.1 mT drive field in a zero applied field. The frequency of the drive was 113 Hz to minimize the distraction from the electricity grid. The critical temperature, T_c was considered to be the onset of the in-phase of the AC-component of the magnetization. It

describes the slope of the magnetization curve and the out-of-phase component energy dissipation during the transition. The width of the transition, ΔT_c, was considered as the temperature difference between 10 % and 90 % of the transition. The schematic diagram of the measured data is shown in figure 7. The difference between magnetic and resistive T_c emerges because in the magnetic measurement the signal is attained from the entire sample whereas the resistive measurements probe only a small part of the superconductor due to a small probing current.

The DC-measurement was used to determine the critical current of the sample at constant temperature as a function of the applied magnetic field perpendicular to the plane of the sample. The J_c was determined at 10 and 77 K to find out J_c using the Bean model, according to equation (2), shown in chapter 1.4.

2.6 Transport measurements

Sample preparation For the transport measurements, the samples were patterned using wet chemical etching. Both for the $J_c(\theta)$ measurements and the measurements in the pulsed magnetic field, a 50 μm stripes were used. Patterning was done in a cleanroom using wet chemical etching technique. In the process, the sample was first coated with positive photoresist which was spread by spinning the sample. The resist was dried in an oven and after that the desired pattern was exposed on the sample using UV light. The exposed sample was then developed in a NaOH solution where all the exposed photoresist was flushed away. The pattern was etched in the H_3PO_4 solution and reaction stopped by using ultrapure water. Finally, the remaining photoresist was removed with acetone.

The etched circuit was checked and the width and height of the stripes measured using atomic force microscopy. After that, the contacts on the sample were made by tapping with indium and the sample was attached to the sample holder with suitable methods, in the $J_c(\theta)$ measurements by a double sided tape and in the pulsed magnet using stearin.

The angular dependence of J_c The critical current was measured using the horizontal rotator probe of the PPMS. In the measurements the voltage drop in a four-wire configuration is monitored as a function of the applied current. To protect the sample, the current is cut down as a critical voltage limit was exceeded. The measurements can be done in an applied field up to 9 T and the sample is rotated in magnetic field in a

maximum Lorentz force configuration, i.e. the current stripe is always perpendicular to the external field.

In [**P1**] the measurements were made between 10–70 K in 10 K steps in the fields of 0.5 T and 1–8 T with 1 T steps. In [**P3**] and [**P5**] only the most relevant fields and temperatures were measured so that still a comprehensive picture of the behaviour could be obtained. The voltage limit for the critical current in all these works was 215 μV/cm. However, the high value does not change the shape of the angular dependencies [91] and it is used to deal with the noise due to the measurement setup.

The resistive measurements of B_{c2} and B_{irr} The resistive measurements of B_{c2} and B_{irr} using PPMS were also done using the horizontal rotator probe in [**P2**]. The sample resistances were measured as a function of temperature in various applied fields between 120 and 40 K using a 10 μA current. The probing current was kept as low as possible not to affect the measured resistivity curve. The measurement was repeated in several external magnetic fields, measuring more densely in the low field regime.

As the measurements were done in constant field, one can obtain T_{irr}, the temperature at which the resistance starts to deviate from zero at a certain magnetic field. An example of a resistive transition scan is shown in figure 7 along with the defined T_c, ΔT_c and B_{irr}. Using the measured curve, a pair of (T,B_{irr}) can be obtained and with all these points, B_{irr} as a function of temperature can be drawn. The voltage limit for the T_{irr} was 1 μV/cm. For B_{c2} the limit was the same as for resistive T_c in zero field, 80 % of the normal state resistivity. This definition was found to give most consistent results and it is also similar to method used in [92].

Measurements for B_{c2} and B_{irr} in pulsed magnetic fields High magnetic fields can be created by short-circuiting a solenoid. The high current in the solenoid creates a strong magnetic field inside the solenoid for a short time. By using pulsed current, for example the effect of Joule heating due to wire resistances can be diminished as compared to ordinary electromagnets. The pulse duration in the measurements in [**P4**] was 8 ms and amplitude up to 30 T. The samples were mounted on the sample holder current stripe perpendicular to the field, i.e. maximum Lorentz force configuration. The measurements were made by recording the $R(B)$ curves, the resistance as a function of applied field. To get high-quality data, for a measurement at 30 T, several lower field pulses were also shot and the final curve is a combination of pulses of different magnitudes. The sample was tilted in 10° steps from 0° ($B||c$ axis of YBCO) to 100°

and probed with a 200 μA current. The measurement temperatures were chosen relative to the magnetically determined T_c, $0.96T_c$ and $0.90T_c$. At extreme angles, 0° and 90°, also points between those temperatures were measured.

In the analysis of the measured $R(B)$ curves, B_{irr} was taken as the point at which the resistivity was 1 % of the normal state resistivity. B_{c2} was defined to be the intersection of two tangents, drawn at the normal state resistivity and to the steepest point of the transition [74, 76].

3 Simulation

3.1 Molecular dynamics simulations

Molecular dynamics is a simulation method to calculate the dynamic evolution of a system using mutual interactions of the units involved in the simulation. At each step, forces on every particle are calculated after which the velocities are updated. This is used to find the new positions of the particles. The molecular dynamics simulation in this thesis uses an equation of motion

$$m_n \mathbf{a}_{n,i} = \mathbf{F}_{\mathrm{tot},n,i}, \tag{6}$$

where m and $\mathbf{a}_{n,i}$ are the mass and acceleration of the nth particle at time i respectively, $\mathbf{F}_{\mathrm{tot},n,i}$ the sum of forces acting on the particle n at the moment i. In the notation, n refers to a particle and i to the moment of time.

There are several possible ways to iterate the system evolution and in this work, the leapfrog algorithm was used. It is equivalent to the velocity Verlet algorithm which estimates velocities using averages between two steps and thus also conserves energy. The position at the moment i is found as (omitting n for clarity)

$$\mathbf{r}_i = \mathbf{r}_{i-1} + \mathbf{v}_{i-1/2}\Delta t, \tag{7}$$

where $\mathbf{r}_{i-1}$ is the position of a particle at step $i-1$, $\mathbf{v}_{i-1/2}$ the speed of a particle at the step $i-1/2$ and Δt the time step in the simulation. The iteration for velocity is done as

$$\mathbf{v}_{i+1/2} = \mathbf{v}_{i-1/2} - \frac{\mathbf{F}_{\mathrm{tot},i}}{m}\Delta t. \tag{8}$$

Since the algorithm uses only half a time steps for velocities, for the calculation on forces at the moment i it has to be defined that $\mathbf{v}_i = \frac{1}{2}(\mathbf{v}_{i-1/2} + \mathbf{v}_{i+1/2})$. To get reasonable results, the time step Δt has to be small enough so that the particle position and velocity do not change too much within one time step.

3.2 Simulation details

In the molecular dynamics simulations presented in [**P5**], the simulation was sliced into 40 layers, perpendicular to YBCO c axis. A schematic picture of the simulation configuration is shown in figure 8. A vortex in the simulation is described by a chain of particles and in every layer there is one vortex particle per vortex. The particles of one vortex are kept together by a spring-like line tension force. Since the line tension

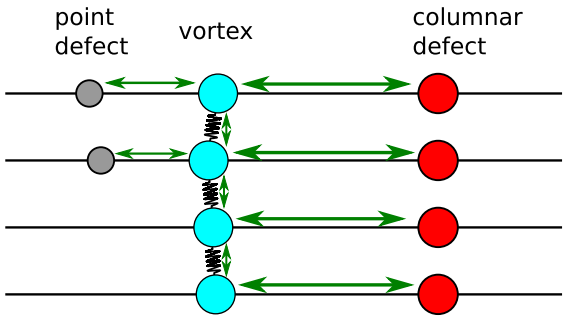

Figure 8. A schematic diagram of the used molecular dynamics model. Vortices are turquoise, point pinning sites grey and rods red. The particles of a vortex are connected with a spring-like force. For visualisation, only four layers are shown and layers contain both rods and dots. Interactions are shown with green arrows.

is the only layer-to-layer force, the model fails at angles close to $B||ab$. At high angles, the vortex–vortex interaction would be needed between adjacent layers as well. Inside each layer a vortex interacts with other vortices and pinning sites. Pinning sites are represented as particles that do not move but have different radii to emphasize their pinning strength. Point defects have radius of 1.5 nm and rod defects are point pinning centres on top of each other in separate layers with a 3 nm radius. To avoid having too many pairwise interactions to be calculated, the only direct interaction between layers is the line tension of a vortex from layer to layer. There are also forces that originate from the angular position of the vortex, line tension and magnetic force, but they are not particle-particle interactions as such. Furthermore, in the layers, parallel to YBCO *ab* plane, vortices are subject to periodic boundary conditions. Thus the vortex that has come out of the sample area will re-enter the sample from the other side. There is no periodicity in the *c* direction and the layer-to-layer forces are applied only from one side in the boundary layers. In the model, the effect of temperature is not included i.e. temperature is 0 K.

The total forces acting on the vortex n is

$$F_{\mathrm{tot},n,i} = \sum \mathbf{f}_{vv} + \sum \mathbf{f}_{vp} + \mathbf{f}_L + \mathbf{f}_l + \mathbf{f}_{\mathrm{magn}} - \eta \mathbf{v}_i, \tag{9}$$

where $\sum \mathbf{f}_{vv}$ is the sum of vortex-vortex forces on a vortex n in a certain layer, $\sum \mathbf{f}_{vp}$ is the sum of forces between vortex n and all pinning sites in a certain layer, $\mathbf{f}_L$ is Lorentz force, $\mathbf{f}_l$ is the force due to line tension, $\mathbf{f}_{\mathrm{magn}}$ is the force due to magnetic field energy and $-\eta \mathbf{v}_i$ is the drag force that vortices experience in superconductors. Additionally,

the mass of a vortex, m, in equation (8) is only an additional parameter to scale the time step and does not represent any physical quantity.

The magnitude of the vortex-vortex force is [93, 94]

$$f_{\mathrm{vv}} = \frac{\varepsilon_0}{\lambda_{ab}} \mathrm{K}_1 \left(\frac{r}{\lambda_{ab}} \right), \tag{10}$$

where ε_0 is the characteristic vortex energy per length, λ the magnetic penetration depth, r the distance between two vortices, K_1 the Bessel function of first kind, first order. The characteristic energy is $\varepsilon_0 = \phi_0^2/(2\pi\mu_0\lambda^2) \approx 2.76 \cdot 10^{11}$ J/m, where ϕ_0 is the magnetic flux quantum and μ_0 the magnetic permeability of free space.

The force between a vortex and a strong pinning site is [16, 95]

$$f_{\mathrm{vp}} = \varepsilon_0 \frac{r r_0^2}{(r^2 + 2\varepsilon_\vartheta \xi_{ab}^2)^2}, \tag{11}$$

where r is the distance of pinning site and vortex, r_0 the radius of the pinning site and ξ the coherence length of YBCO and ε_ϑ is the angle-dependent Blatter scaling parameter introduced in chapter 1.4. The scaling parameter is needed when the vortex is not parallel to the YBCO c axis and it scales the ξ appropriately. The pinning site radius of 3 nm and 1.5 nm was used for rod and dot pinning sites, respectively. Although equation (11) is derived for pinning sites with $r_0 \ll \sqrt{2}\xi$, it is a reasonably good approximation also for pinning sites with $r_0 > \sqrt{2}\xi$, especially at large distances. More importantly, it does not diverge at any distance.

The Lorentz force is $f_L = |\boldsymbol{\phi_0} \times \mathbf{J}_\mathrm{c}| = \phi_0 J_\mathrm{c}$. The equality holds true because the current is always kept perpendicular to the magnetic field. The drag coefficient η is [96]

$$\eta = \frac{\phi_0 B_{\mathrm{c}2}}{\rho_n}, \tag{12}$$

where ρ_n is the normal state resistivity of YBCO, $5.3 \cdot 10^{-7}$ Ωm [**P4**] and the upper critical field, $B_{\mathrm{c}2}$, is 27 T [97] at 77 K in the c direction.

The line tension e_l can be calculated by starting from the vortex line energy [16]

$$e_l = \varepsilon_0 \varepsilon_\vartheta L \ln \frac{\lambda}{\varepsilon_\vartheta \xi}, \tag{13}$$

where L is the length of a vortex. Considering that $\varepsilon_\vartheta = \varepsilon_\vartheta(\theta(\mathbf{r}))$, where $\mathbf{r}$ is the r is the displacement in the ab plane of vortex particle from layer to layer projected onto layer, and that $\mathbf{f}_l = -\nabla e_l$ we can obtain the force. Writing this into a series around $r = 0$ yields the magnitude of the line tension in the ab plane to be

$$f_l = -\frac{\varepsilon_0 r(\gamma^2 - 1 + \ln\kappa)}{d_z \gamma^2 \sqrt{d_z^2 + r^2}}, \tag{14}$$

where d_z the distance between successive layers. Due to the layered structure of the simulation, particles forming a vortex are allowed to move only in the *ab* plane and thus only the line tension component parallel to the *ab* plane is considered.

The force restoring the vortex parallel to the external field is calculated by differentiating the energy of a vortex in magnetic field, e, tilted an angle φ from the direction of the field,

$$e_{\mathrm{magn}} = -\phi_0 B_{\mathrm{ext}} \cos\varphi/\mu_0, \tag{15}$$

where B_{ext} is the magnitude of the external magnetic field. Differentiating this yields the force $f_{\mathrm{magn}} = \phi_0\mu_0 B_{\mathrm{ext}} \sin\varphi \frac{\mathrm{d}\varphi}{\mathrm{d}r}$, where φ is the angle between vortex and the external field. Like in the case of line tension, also here only the component parallel to the *ab* plane is considered.

The distribution of the nanorods in the simulations was taken from experimentally determined distribution [21] but for computational reasons the separation between the rods was doubled. This does not have any effect on the shape of the $J_{\mathrm{c}}(\theta)$ curves. In contrast, the distribution of the dot pinning sites was random. Only rod or dot pinning sites were used in a layer so that it was possible to see the effect of those particular defects. In the samples that had more than one entity of rod layers, the position of the rods was varied slightly in the next entity compared to the first rod positions. This was done due to the experimental results of [**P5**] that BZO rods in the sample did not grow on top of each other in different layers. Always, the total number of layers was 40 and in the multilayer samples there were equal number of rod and dot layers. Depending on the desired configuration, the thickness and number of these layers were varied, like in the experimental samples in [**P5**]. The number of the vortices was determined by the field strength according to equation $B = n\phi_0$, where n is the vortex density. The size of the calculation area was 200 nm times 260 nm, resulting in 19 vortices at 0.75 T field.

The critical current was iterated by the bisection method. The simulation was run with one current and the current in the following iteration was adjusted according to the stability of the system. The system was considered stable if the average positions of the vortices have not moved more than double the coherence length, ξ_{ab}, compared to the position at 1000 and 500 iterations ago. The average of the vortex position was calculated over all the layers. Additionally, if this condition was not fulfilled, the average speed of the vortices was checked. A vortex was considered stable if its current speed was below 200 m/s. This limit was chosen based on experience and as the speeds of the vortices are defined by the arbitrary mass of the vortex, the used time step and the drag parameter η, and thus the speed limit is completely arbitrary. Both the position and

speed stability were checked with regular intervals during the simulation. To make the calculations stabilize faster, the vortices were initially set into hexagonal lattice [16].

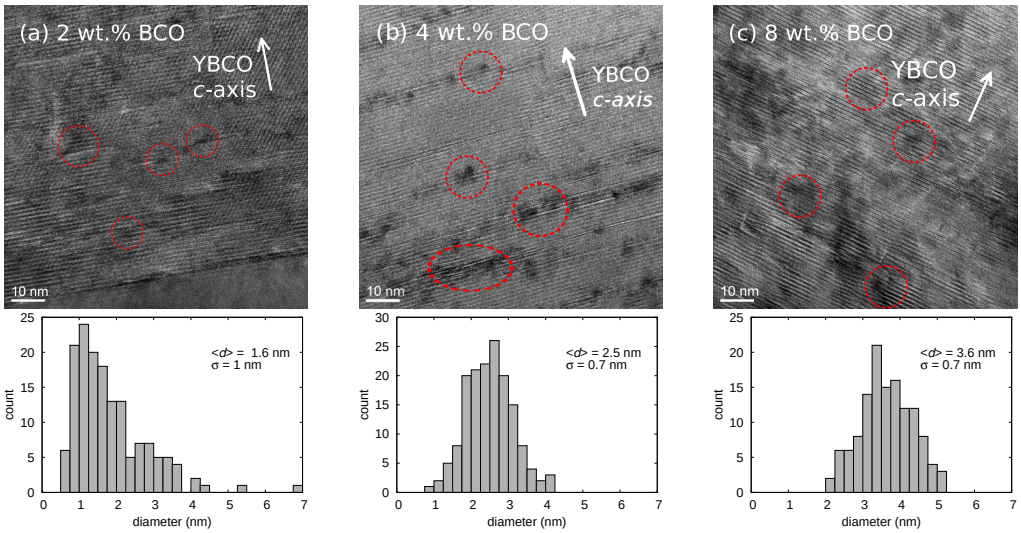

Figure 9. Cross-sectional TEM images of (a) 2 wt.%, (b) 4 wt.% and (c) 8 wt.% BCO doped samples along with the size distribution of the BCO particles in each case. Red dashed areas point some of the particles. [**P3**,**P4**]

4 Structural properties of doped samples

4.1 BCO doped YBCO

Before this thesis work, it was suggested that BCO forms small particles with 2 nm diameter, as deduced by broad BCO (002) XRD peak [67]. The same peak is also seen at $\theta - 2\theta$ scan of the $(00l)$ peaks [**P3**]. This is the only BCO peak seen which suggests that BCO has grown topotaxially. The topotaxial growth also causes smaller strain, as compared to non-epitaxial BCO particles grown by CSD [76]. Due to the small size of the particles and thus wide and weak XRD peaks, no exact analyses of the BCO (002) and (110) peaks could be done.

The TEM measurements confirm the presence of small, spherical particles with 1.6, 2.5 and 3.6 nm in average diameter in 2, 4 and 8 wt.% doped samples, respectively. The cross-sectional images along with the size distribution of the BCO particles is shown in figure 9. The particles are much smaller than BCO particles in CSD grown YBCO [76] that are 50 nm in diameter. The BCO particles are also smaller than BZO rods [**P1**],[21]. The BCO particles are dispersive, but in some local areas they are clustered into lines in the direction of the YBCO *ab* planes, as the figure 9 (b) suggests. Also, with higher concentration, the particles are more aggregative, seen especially in 8 wt-% doped sample

Table 1. The basic structural properties of the BCO doped samples [**P3**].

BCO concentration	0 wt.%	2 wt.%	4 wt.%	6 wt.%	8 wt.%
FWHM (005) (°)	0.17	0.19	0.23	0.24	0.28
FWHM rc(005) (°)	0.15	0.19	0.21	0.34	0.38
c-axis (Å)	11.679	11.685	11.693	11.704	11.716
r_c (nm)	28	23	20	13	11

in figure 9 (c). Furthermore, BCO causes a lot of stacking faults, seen as long line-type contrast in the TEM images.

BCO creates a lot of distortion in the YBCO lattice which can be most clearly seen from the XRD results of table 1. The FWHM of YBCO (005) peak increases from 0.17° to 0.28° with increasing BCO concentration. Also, the FWHM of the YBCO (005) rocking curve grows from 0.15° to 0.38° which implies that the out-of-plane tilt increases with BCO concentration. Furthermore, the length of the YBCO c axis grows from 11.68 Å to 11.72Å which is a typical consequence of dopant addition [98, 99]. In total, the dopant increases both micro- and macrostrain and also the splay in the direction of the c axis. This all is reflected into the correlation length, r_c, calculated as presented in [89]. The correlation length describes the distance that the atom positions are correlated and it decreases from 28 nm to 11 nm in the c direction as a result of BCO doping. Furthermore, according to the XRD scans of YBCO (102), no a axis oriented grains were formed. The trends are similar than seen in [67] but probably even more clear. However, compared to that, no chaotic twinning was observed which may be due to slightly different deposition conditions.

4.2 BZO doped YBCO deposited at different temperatures

The effect of the deposition temperature, T_{dep}, was studied by making 5 wt.% BZO doped YBCO thin films with T_{dep} ranging from 700 °C to 850 °C in 25 °C steps. The oxygenation temperature was always 50 °C below T_{dep}. Based on the properties of the angular dependencies of the critical current, the samples were divided into three categories. The low- and mid-T boundary is about at 700–725 °C and mid- and high-T boundary is at 800–825 °C. Films within the same category have similar structural and superconducting properties and thus the categorization could be used.

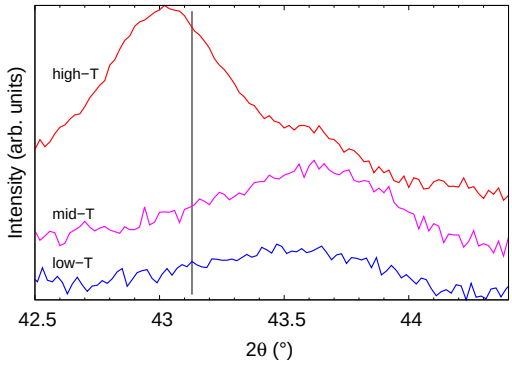

Figure 10. The $\theta - 2\theta$ diffractogram of BZO (002) peak in different sample regimes of 5 wt.% BZO doped YBCO samples. The black line corresponds to BZO (002) bulk peak [50]. [**P1**]

Table 2. The properties of BZO columns at different deposition temperature regimes.

regime	rod diameter (nm)	rod alignment
low-T	4.5–5.5	splayed 15–30°
mid-T	6–7	well-aligned, continuous
high-T	4–8	well-aligned but shorter than in mid-T

The twin structure is most clearly seen in the high-T samples, but the width of the YBCO (212) peak set is approximately the same in all categories. This suggests that the high-T samples are most relaxed. However, the FWHM of the YBCO (005) rocking curves does not have any correlation with T_{dep}, it varies approximately between 0.20 and 0.30, which is similar than before [100, 101]. Also, the intensity ratios of the peaks in all the samples are $I(005)/I(007)$ between 7 and 10 and $I(005)/I(004) < 20$ and therefore it can be concluded that the samples are properly oxygenated with $\delta < 0.1$ [73].

The BZO rod structure depends clearly on the deposition temperature. The BZO (002) peak is seen roughly at $2\theta = 43.6°$, but in the high-T samples emerges a strong peak at 43.0° which is closer to the bulk value of BZO (figure 10). Even though the FWHMs of the BZO peaks could not be reliably compared due to small intensities, this evolution suggests that the BZO is much less strained in the high-T samples.

In the TEM images of the samples (figure 11) it is seen that the low-T samples have splayed nanocolumns with 4.5–5.5 nm diameter and splaying angle of 15–30°. On the

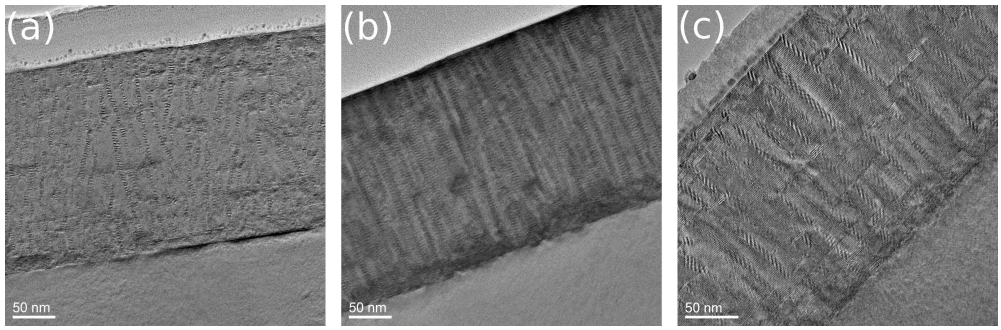

Figure 11. Cross-sectional TEM images of (a) low-T, (b) mid-T and (c) high-T samples. The BZO content in the samples is 5 wt.%. [**P1**]

other hand, the mid-T samples have well-aligned nanocolumns, with 6–7 nm width and separation of 10–15 nm. Also the high-T samples have well-aligned, straight columns with 4–8 nm diameter but they are shorter. The high-T sample contains also a lot of stacking faults. The results are summarized in table 2. The diameters are taken from a single image in each cases and thus it cannot be reliably said that there are significant differences in the rod diameters in different regimes. Previously, it has been found that the rod diameter does not change with T_{dep} [78] whereas the BZO rods in $SmBa_2Cu_3O_y$ showed a clear increase in the rod diameter with T_{dep} [102]. These even controversial results suggest that the rod growth process is not straightforward.

Furthermore, according to the energy-dispersive X-ray analysis, the rods do not consist merely of BZO but there are also Y and Cu atoms. The extra atoms also explain the change seen in the lattice parameters of BZO which thus accommodates itself into the YBCO matrix. However, in the high-T regime the rods are less strained and judging by the lattice parameter, also more pure.

4.3 Multilayer structures

The joint effect of differently doped YBCO layers were studied by making a set of samples of roughly equal thicknesses with different number of 4 wt.% BCO or 4 wt.% BZO doped YBCO layers. The schematic diagram and the names of the samples are shown in figure 12. The samples are free from impurities, as can be concluded from the $\theta - 2\theta$ diffractograms of the samples having no impurity peaks (figure 13). The BZO (002) is seen roughly at 43.5° which suggests that it is crystalline. Also, the wide BCO (002) peak at 41° suggests crystallized growth of the small BZO particles as well.

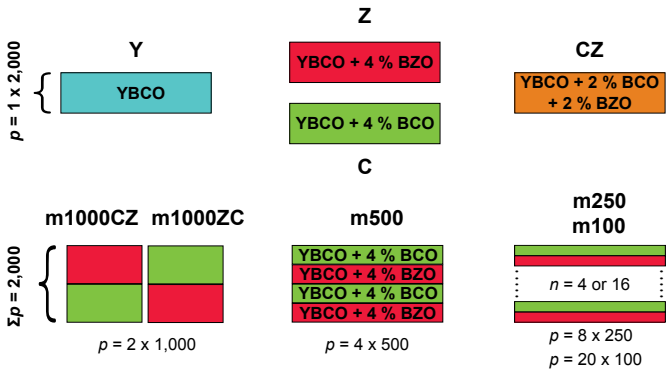

Figure 12. Schematic diagram of the deposited multilayer samples. Each pulse produces approximately 0.1 nm of YBCO. [**P5**]

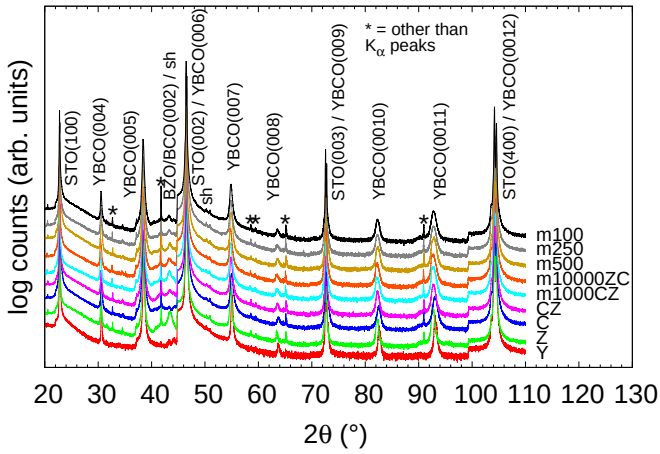

Figure 13. The $\theta - 2\theta$ diffractogram of the multilayer samples. The curves have been shifted for clarity. [**P5**, SI]

Table 3. Most important structural properties of the multilayer samples measured by XRD. [**P5**, SI]

sample	FWHM YBCO (005) (°)	c axis length (Å)	r_c (Å)
Y	0.15	11.680	124
C	0.28	11.722	74
Z	0.10	11.727	154
CZ	0.26	11.729	76
m1000CZ	0.29	11.719	88
m1000ZC	0.29	11.730	96
m500	0.29	11.713	98
m250	0.29	11.724	88
m100	0.25	11.721	95

Also in this series, it is seen that the dopant increases the c parameter, like in [**P3**] and [**P4**]. However, there is no correlation with the doped layer thickness, and small variation in the parameters is due to sample-to-sample variation. All the doped samples have c parameter of at least 11.71 Å (table 3). The correlation length is between 8 and 10 nm, but Y and Z have higher value. Their better crystal quality is also reflected into FWHM of the YBCO (005) peak. The Y and Z have 0.15° and 0.10°, respectively whereas other samples have FWHM of almost 0.30°. All the samples are biaxially twinned apart from CZ and none of them have a axis oriented grains.

The structure of m1000ZC, m250 m100 and CZ were further studied using TEM. The m1000ZC has rods with a diameter of (5±1) nm and a distance of (10±1) nm. The BCO layer in the sample has point-like particles with (3±1) diameter. The dimensions of the dopants are similar to values seen in [**P1**,**P3**,**P4**]. The rods at m250 have same kind of rods (figure 14 (a)), although they are shorter due to smaller layer thickness. In m100 the rods have the same thickness and distribution but they are straight. Additionally, the rods have not grown on top of each other unlike in BSO doped YBCO with undoped spacer layer [59] where BSO rods were formed on top of each other. However, the spacer BCO doped layer is very disturbed [**P3**],[67], and thus this likely disturbs the strain-mediated growth of the rod structure [79].

The BCO layer in m1000ZC also contains strained zones, basal dislocations, Y124 intergrowths and dislocations (figure 14 (b)). Additionally the BCO layer contains stacking faults that are very long. Stacking faults are also seen in BZO doped layers

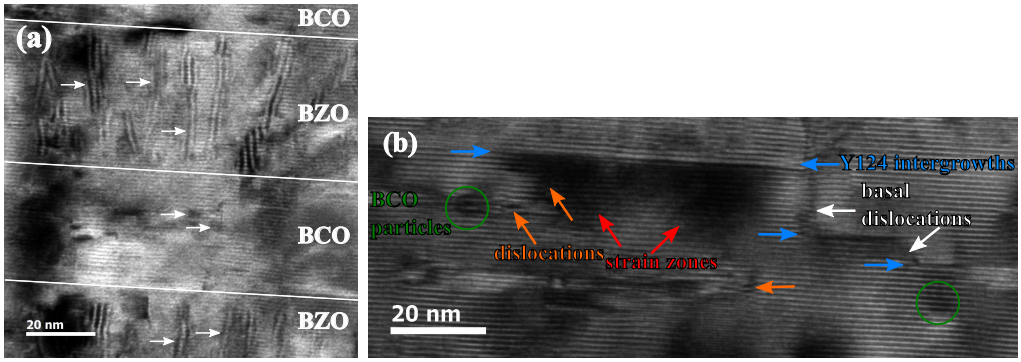

Figure 14. (a) The TEM image of m250 and (b) different defects seen in the BCO doped layer of the m1000ZC. [**P5**;**P5**, SI]

but they are shorter. In general, the BCO-BZO layer interface is good, although there are some dislocations to accommodate the strain due to dopant change. Sometimes there is accumulation of BCO, partly above BZO rods. On YBCO-substrate interface, there are layers of uncrystallized YBCO, for example m1000ZC has a 15–20nm layer of unordered YBCO at the interface and m250 has 6 nm. In m250 there are also small twin regions which implies a larger number of twin boundaries. The mixed dopant sample CZ has both good and bad areas, but as a whole it does not have a well-ordered crystal structure. Even though YBCO contains many defects, the effect of columnar rods on pinning is still clearly strongest [22, 103].

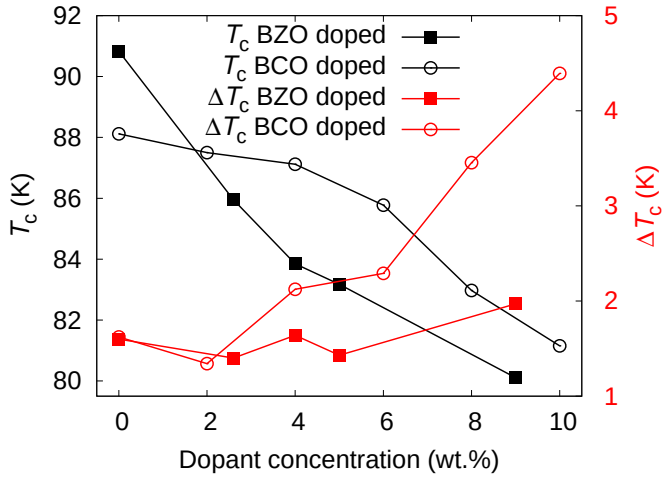

Figure 15. The critical temperature, T_c, and the width of the transition, ΔT_c, in BCO and BZO doped samples. The BZO doped samples are deposited at 770 °C and BCO doped at 750 °C. [**P2**] and [**P3**]

5 Superconducting properties of doped samples

5.1 The critical temperatures

Doping YBCO, in general, causes the critical temperature, T_c, to drop (figure 15), as seen also before (for example [21]). The magnetic onset T_c in BZO doped YBCO [**P2**] deposited at 770 °C, which results in straight columns, decreases from 91.5 K to 81 K with the increasing dopant concentration from 0 to 9 wt.% of dopant. The width of the transition is between 1 and 2 K with a slight increase in the highest concentration. The increased concentration causes also a very tiny phase of YBCO with higher T_c which can be detrimental to measurements with small probing current as it shows a transition consisting of several parts. However, if needed, the phase can be compensated by using higher deposition temperature [23].

On BCO doped samples, deposited at optimal 750 °C, the T_c decreases from 88 K to 83 K with concentration change from 0 to 10 % (figure 15). However, unlike on BZO doped samples, the transition broadens significantly from 1.6 K to 3.5 K with increasing concentration, as measured in [**P3**]. The imperfections created by the dopant cause deviations from the ideal crystal structure and thus the T_c is decreased. However, compared to BZO, BCO causes larger strain and distortion, probably due to larger lattice parameter than BZO, as can be concluded from the FWHM of the YBCO (005) peaks [**P5**,

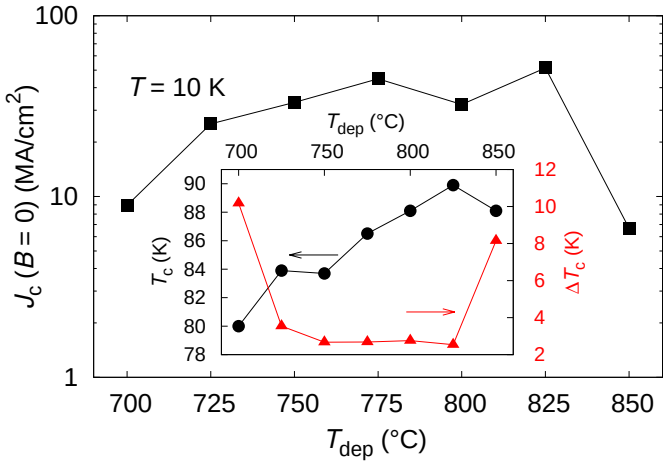

Figure 16. The evolution of the self-field critical current density at $B||c$ axis of YBCO at 10 K. The BZO content is 5 wt.%. The inset shows the critical temperature, T_c, and the width of the transition, ΔT_c. [**P1**]

SI]. Because BCO forms small particles, the interface area between dopant and YBCO is much larger than with BZO rods which might explain the increase in ΔT_c. The additional distortion can also be seen as longer stacking faults in BCO doped YBCO than in BZO doped. Furthermore, the BCO and BZO doped samples are from different sample batch and comparisons can be reliably made only within a certain batch. Additionally, the sample-to-sample variation adds uncertainty in direct comparison of the results.

The critical temperature can also be measured resistively. The trend of the resistively measured transition of BZO doped samples is similar to magnetically measured [**P2**]. However, the decrease with increasing concentration is only from 93 K to 88 K but the width of the transition changes from 1 K to 6 K. In magnetic measurements the transition curve reflects the properties of the entire sample but the small probing current in the resistive measurements is able to use only the percolatively best linked parts of the sample and thus different results can be seen.

The critical temperature of 5 wt.% BZO doped samples as a function of the deposition temperature evolves from 80 K of the 700 °C sample to almost 90 K in the high-T samples with a slight decrease in too high T_{dep} (figure 16). With the lowest and highest deposition temperature, ΔT_c is close to 10 K but in the mid-T samples between 2 K and 3 K. That is to say, both extreme temperatures degrade the film quality remarkably, although the high T_{dep} helps to recover T_c back to the value of the undoped sample [87].

Table 4. The superconducting properties of the BCO doped samples. [**P3**]

BCO concentration	0 wt.%	2 wt.%	4 wt.%	6 wt.%	8 wt.%
T_c (K)	88.1	87.5	87.1	85.8	83.0
ΔT_c(K)	1.6	1.3	2.1	2.3	3.5
T = 10 K					
J_c(0 T) (MA/cm^2)	54	53	40	28	22
J_c(3 T) (MA/cm^2)	7.3	8.9	7.9	6.5	5.8
B^* (mT)	81	95	89	116	127
α	0.44	0.42	0.38	0.36	0.33
T = 77 K					
J_c(0 T) (MA/cm^2)	3.5	3.4	2.0	0.75	0.20
B^* (mT)	5.8	6.6	5.1	4.6	2.7
α	0.25	0.23	0.23	0.25	0.29

The small decrease of the T_c observed also in [87] can be explained by increased amount of stacking faults and thus slightly decreased crystalline quality. Furthermore, according to the analysis of the peak ratio, the films are properly oxygenated and it is not the reason for the T_c decrease.

The multilayer structures in [**P5**] do not affect the critical temperature. The values are between 87.7 K and 88.6 K without a correlation with the number of the deposited layers. Only the mixed dopant sample, CZ has a lower T_c with 85.0 K. The ΔT_c is roughly 2 K or below, only CZ has a higher value, which again reflects its distortion.

5.2 Dopant morphology and $J_c(B, \theta)$

5.2.1 Spherical particles

The effect of spherical non-superconducting BCO particles on J_c depends clearly on the dopant concentration, as studied in [**P3**]. At 10 K the self-field J_c deteriorates from 54 MA/cm^2 to 22 MA/cm^2 with increasing dopant concentration (see table 4 and figure 17). The in-field value at 3 T is highest on 2 and 4 wt.% doped samples. At 77 K the behaviour is similar, the self-field J_c decreases from 3.5 MA/cm^2 to 0.20 MA/cm^2

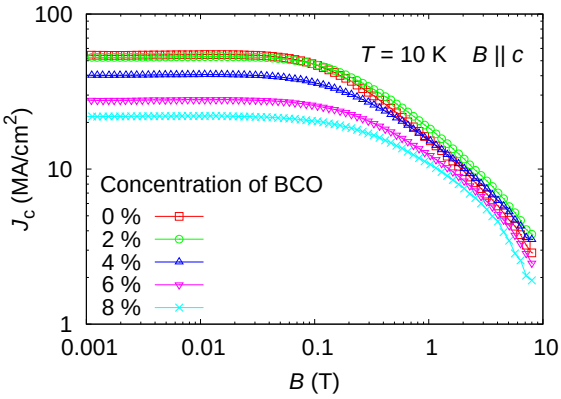

Figure 17. The magnetic field dependence of J_c of BCO doped samples, measured at 10 K, $B||c$ axis of YBCO. [**P3**]

which is also similar to trends seen before on BCO doped samples [67, 104]. However, when looking at the fit results of α in $J_c \propto B^{-\alpha}$, the 8 wt.% sample has the lowest α, 0.33. This implies the smallest reduction of J_c in magnetic field. The value of α is slightly larger than that of the BZO doped YBCO which has α roughly between 0.25 and 0.30 [21, 53]. Furthermore, because larger BCO concentration implies larger particle radius, the pinning force increases and thus α decreases with higher BCO content [22]. At 77 K none of the BCO doped samples is good any more and the sample with the largest concentration has the largest α.

Like α, the accommodation field, B^* at 10 K has also the best value of 127 mT on the 8 wt.% sample (table 4) and the values decrease almost linearly with BCO concentration. This is similar to the behaviour of B^* on the BZO doped samples at 10 K at low concentrations, but above 5.7 wt.% doping level, the B^* of the BZO doped samples starts to drop. However, it is noteworthy that the maximum value of B^* at 10 K on BZO doped samples is much higher, 500 mT, than on BCO doped or undoped YBCO [21]. At 77 K the undoped sample has the highest B^*, 5.8 mT (table 4). The change is similar in BZO doped YBCO as well, since at 60 K the undoped sample has the highest value, slightly below 100 mT [21]. This is clearly higher than that of the BCO doped samples which is caused by, in addition to different pinning landscape, lower measurement temperature.

The obtained values can be explained with the behaviour of vortices. At 10 K, the ξ_{ab}, and thus the vortex diameter, is of the same order as the defects. Near T_c the vortices are larger and the defects do not create strong enough pinning force. For the

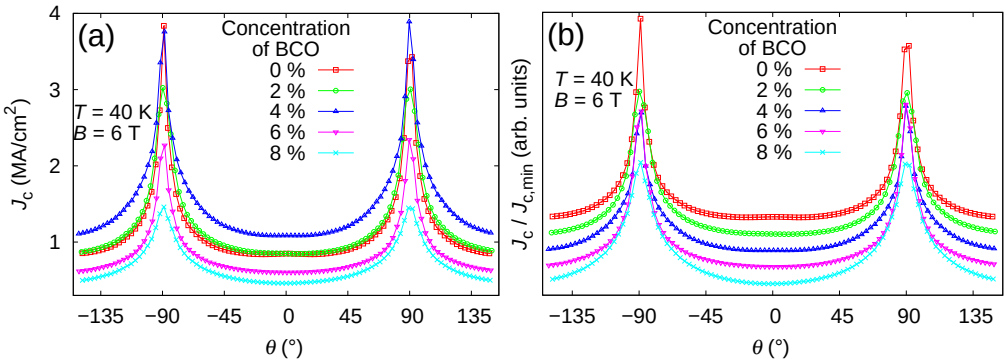

Figure 18. (a) The angular dependencies of J_c of the BCO doped samples at 40 K and 6 T. (b) The same data scaled with its minimum value and shifted for clarity to emphasize the shape of the curves. [**P3**]

same reason, the BZO rods work best at low temperatures, far away from T_c, as seen for example in the behaviour of the accommodation field. Additionally, the dopants also create defects in the YBCO matrix, increasing the effective size of the dots and this makes it possible to see enhancements also near T_c. On the other hand, the decrease of T_c due to the dopants also affects the J_c values decreasingly and thus the optimization is not straightforward. As a simplification, it can be assumed that the increased pinning capability at higher concentrations is due to the larger non-superconducting particles and thus larger pinning forces.

The spherical particles do not create easily recognizable effects on the angular dependence of the critical current, $J_c(\theta)$, (figure 18 (a)) and the 4 % sample has the highest J_c values throughout all angles at 40 K and 6 T field. The shapes of the curves can best be compared by using a scaled plot (figure 18 (b)). The most notable change is the broadening of the *ab* peak (at $\theta = \pm 90°$) with increasing concentration. The curves measured far away from T_c, at 10 and 40 K, are very much alike, 10 K has only higher J_c values. The measured data at 40 K, 6 T is shown in figure 18 since 40 K is technologically more important than 10 K [32]. The tiny *c* peak at $\theta = 0°$ is likely due to pinning into twin domains or misfit dislocations.

As the measurement temperature is increased, the *ab* peak becomes wider (figure 19 inset) and the effect is best seen near T_c. However, due to their small size, BCO affects most efficiently at low temperatures, where vortices are small. At low temperatures the intrinsic pinning [105] produces a rather sharp peak, with magnetic field tilt smaller than the trapping angle [16, 106] but at higher temperatures the peak is broadened due

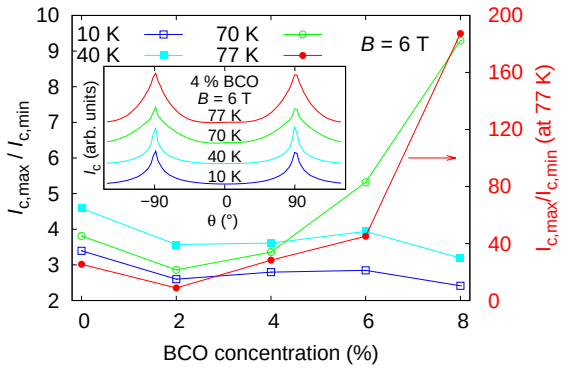

Figure 19. The $I_{c,max}/I_{c,min}$ as a function of the BCO dopant concentration at different temperatures. The scale for the 77 K data is on the right. The inset shows the $J_c(\theta)$ of 4 wt.% doped sample measured at 6 T and at different temperatures. [**P3**]

to smoothing of the pinning potential by thermal fluctuations. The peak is also wider at lower fields as the vortex–vortex interactions are small and the vortices are more free to choose the lowest energy path.

The anisotropy of the $J_c(\theta)$ curves was quantified by calculating $I_{c,max}/I_{c,min}$ as a function of the BCO concentration (figure 19). Due to the shape of the curves, the ratio is very close to the value $I_c(90°)/I_c(0°)$. At 6 T and 10 K the value changes from 3.5 to 2.5 with increasing BCO content and at 40 K from 5.5 to 3.5. The values are much lower than on chemically deposited BZO doped samples that contain large spherical particles [107]. At higher temperatures, the $I_{c,min}$ is close to zero especially on high concentrations and thus the ratios become very high. All in all, the ratio is much smaller at 1 T field, between 1.3 and 2, without correlation with dopant concentration or temperature.

The anisotropy of the $J_c(\theta)$ curves was also described using Blatter scaling -like J_c which has the same form as $J_{c,rand}(\theta)$ in equation (4). The fitting is done by concentrating the area around 0° but at 90°, the peak of the fitting function is not sharp enough [**P3**]. The deviation of the data from ideal sample with isotropic pinning centres is partly caused by non-isotropic defects, like stacking faults and the clusterization of the BCO particles. Thus the obtained anisotropy parameters have to be considered as effective because J_c depends also on extrinsic properties, like flux pinning landscape. As fitted on 40 K, 1 T data, the fit yields γ_{eff} 1.28…1.71. Similar values have been obtained for BZO doped films made by PLD [108] and CSD [82].

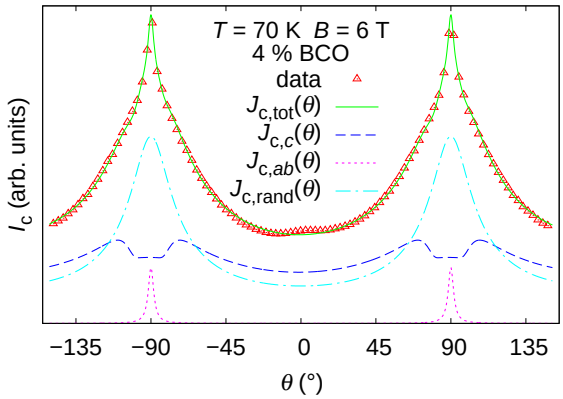

Figure 20. The vortex path model fitted on $J_c(\theta)$of the 4 wt.% BCO containing sample at 70 K and 6 T. [**P3**]

The $J_c(\theta)$ data on the 4 wt.% containing sample at 70 K, 6 T shows *ab* peak with two separate parts (figure 20). A sharp peak is likely due to stacking faults and a wider peak due to clustered BCO particles combined with YBCO anisotropy. The data was also fitted using the vortex path model which has more constituents than the mere Blatter scaling. The model succeeds in describing the data, both the wide and the sharp peak. The variation of the vortex step length is large and thus no *c* peak seen at $\theta = 0°$. The random pinning part, $J_{c,rand}(\theta)$, is smaller than the entire $J_{c,tot}(\theta)$ and therefore it can be concluded that also anisotropic defects affect pinning at $\theta = 0°$. The $J_{c,c}(\theta)$ has shoulders around the *ab* peaks because the variation of the steps that vortices take, is large (i.e. $\Gamma > 1$, see p. 8). This is probably due to the random distribution of the BCO particles.

5.2.2 Columnar defects

The columnar structure can be controlled e.g. by deposition temperature and by creating multilayer structure that will define the length of the rods (see chapter 4). When the rods are controlled by varying the T_{dep}, the behaviour of the self-field J_c follows same trend as T_c. At 10 K, J_c rises up to 30–40 MA/cm^2 but drops again with too high deposition temperature (figure 16). The better ordered rods in the mid-T samples and a well ordered YBCO lattice enable the high J_c values. In the high-T samples, there are a lot of stacking faults which degrades the film quality. The behaviour of the in-field values of J_c is rather similar to the self-field values. At 77 K, however, the self-field values are affected by T_c and ΔT_c, but a maximum of J_c can also be seen there. The

results are in line with previous studies, where a monotonic increase of J_c with T_{dep} was observed [78]. In BZO + Y_2O_3 co-doped samples a maximum J_c was found with T_{dep} of 800 °C [69]. Similar trends have also been found for undoped YBCO [44, 85]. That is to say, the deposition temperature affects the structure of both YBCO and BZO and that is reflected into the superconducting properties of the samples. Additionally, too high T_{dep} degrades the sample properties.

The accommodation field at 10 K decreases almost linearly from 400 mT to 100 mT with increasing deposition temperature. At 77 K the trend is, however, opposite and the B^* for 700 °C sample is 2 mT and 7 mT for the 850 °C sample. The splayed and short rods in the low-T samples are good for pinning at low magnetic field and vortices can easily maximize their mutual distance by utilizing them. In the mid- and high-T samples vortices have less freedom to optimize their mutual distances and thus the field at which vortex–vortex interaction lowers J_c is decreased. Additionally, the B^* at 77 K is greatly affected by the proximity of T_c. Commonly it can be found that the shape of $J_c(B)$ stays roughly the same at different measurement temperatures far away from T_c [109, 110] although the absolute value drops linearly with rising measurement temperature.

The α, describing the decay of J_c in magnetic field, is 0.35 at 10 K for low- and high-T samples but between 0.15 and 0.20 in the mid-T samples. Judged by this, the mid-T has best in-field properties. At 77 K the mid-T samples have still the lowest value, although it is larger than at 10 K. Using Ginzburg-Landau simulations, it has been found that the smallest α is related to the largest rod diameter [23]. However, in this thesis no clear differences in the diameters were observed. Thus it cannot be concluded that the size of the rods would cause the differences in α but other mechanisms, like the rod length and splay, are likely to affect. The comparison of the α values is further complicated by the shape of the $J_c(B)$ curves. They are not strictly linear above B^*, which creates uncertainty in the fitting procedure.

The different nature of the columnar defects in the samples made at different deposition temperatures is reflected into very different $J_c(\theta)$ curves (figure 21 (a)). To ease the comparison with BCO doped samples, data measured at 40 K is shown. Furthermore, the shape of the $J_c(\theta)$ does not either change remarkably as long as it is measured far enough from T_c. The short and splayed rods in the low-T samples are not capable to pin strongly enough to produce a *c* peak. Going from low-T to mid-T, a wide peak appears at $\theta = 0°$ (*c* peak), evolving from a double peak between the low- and mid-T samples. At that border, the rod splay of the low-T samples has started to decrease and rods become more continuous, still giving a double peak. At the border between mid- and

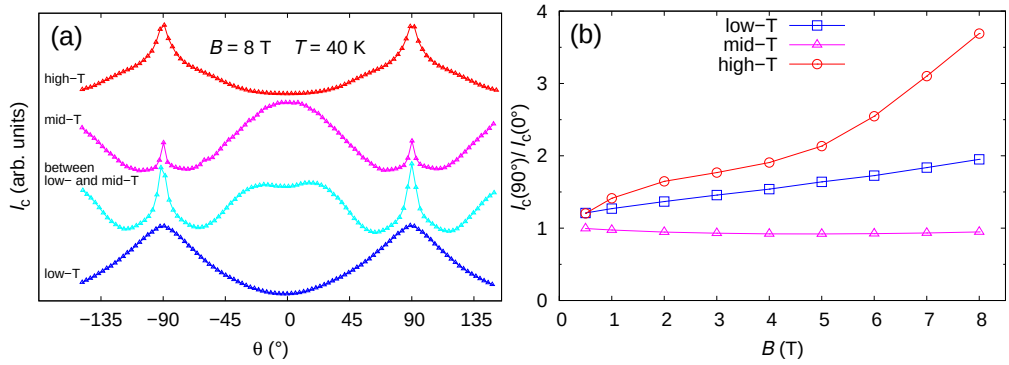

Figure 21. (a) The measured $J_c(\theta)$ curves at 40 K, 8 T on different deposition temperature regimes, BZO content being 5 wt.%. (b) The ratio $I_c(90°)/I_c(0°)$ on the different sample ranges at 40 K. [**P1**]

high-T samples, the *c* peak disappears again. The shorter rods and increased number of stacking faults change the pinning landscape in the *c* direction and thus no *c* peaks are seen. The dislocations and twin boundaries present in the sample are not strong enough to make the *c* peak by themselves.

The *c* peak is most clearly seen at higher fields but at all measurement temperatures which means that the defect structure is capable to pin well at low fields also at angles between 0° and 90°. This could be related to the nanosized PLD target used in the deposition [111]. If there are more vortices than pinning sites, the *c* peak disappears at high measurement temperatures [112]. However, using the data from figure 9, it can be concluded that the defect density is roughly 4400 μm^{-2} with the rod separation of 15 nm and assuming square lattice for the rods. This corresponds to a vortex density at 9.2 T and thus the *c* peak should not disappear in the measured field range.

The *ab* peak, i.e. peak at $\theta = \pm 90°$, behaves entirely differently. On the low-T samples, the shape of the curves is independent of the field. On the mid-T samples, there is first a dip but in the higher fields, the decay of the J_c is smaller at $\theta = \pm 90°$ but larger around it. Thus the peak becomes relatively stronger at higher fields. This is likely due to the large number of stacking faults that pin vortices in that field direction. Wang *et al.* [110] argue that ordered rods cause distortion in the *ab* planes and thus the J_c becomes weaker in that direction. This could explain the deterioration of the *ab* peak from low- to mid-T samples.

The relative decrease of J_c at the same angle with field increase from 0.5 T to 8 T is roughly 80 % on the low-T sample throughout the entire angular range. In the mid-T,

the same drop is 18 % in the *c* direction and 22 % in the *ab* direction. This means that straight and continuous rods are also important for pinning as the field is perpendicular to them. Pinning in the high-T sample is clearly improved in the *ab* direction. Drop in that direction is only 23 % but 75 % in the *c* direction. This may be due to stacking faults and short rods seen in the high-T samples.

Anisotropy is more precisely quantified using the ratio $I_c(90°)/I_c(0°)$ (figure 21 (b)). The more isotropic the sample is, the closer to one is the ratio. The most isotropic samples using this measure are the mid-T samples. The ratio is much higher on the low- and high-T samples, increasing with field. In the low-T samples, the shape of the $J_c(\theta)$ curves is roughly independent of the field. However, the ratios are high because a rather small absolute drop is relatively measured high due to low I_c values. The ratios seen here are remarkably smaller than for the BCO doped samples in the figure 19. This suggests that even non-optimal BZO decreases the anisotropy more than BCO doping. However, one has to keep in mind that this ratio is not the optimal measure of anisotropy for samples with a *c* peak.

At low deposition temperature, the rods are more like spherical particles and not correlated. In such case, no *c* peak can be seen [113]. However, the defects are still much stronger than mere point pinning centres. Furthermore, the evolvement of the *c* peak occurs in a rather narrow T_{dep} window which means that the rod formation is rather sensitive to the correct deposition temperature. Wang *et al.* [110] saw the appearance of a single *c* peak by using a 20 °C higher T_{dep} than on sample without a *c* peak. Similarly to our study, more continuous rods are attained with higher T_{dep} [69, 78]. In these studies, however, the disappearance of the *c* peak was not seen at high T_{dep}. This is likely due to smaller T_{dep} window. All in all, there seems to be certain range of T_{dep} where the rod formation probability is highest.

To find out the vortex behaviour inside the YBCO matrix, the vortex path model was fitted to the measured angular data. The procedure is similar to the BCO samples presented above with the exception of using $\gamma = 3.4$ [74]. From the fits, the FWHM of the *c* peaks were calculated (figure 22). If the obtained value is $\lesssim 55°$, an actual peak can be seen, otherwise not. Before the peak disappears in the high-T range due to high T_{dep}, the FWHM of the *c* peak decreases with increasing field down to 45° at 8 T. Usually, the FWHM is around 55° on the mid-T range with only a slight decrease in the value with field. The large FWHM is caused by large Γ_G or Γ_L in equation (5). They are reflected as a contribution near *ab* peak or at *ab*, depending whether Γ_G or Γ_L is large [27, 28] and by suitable combination of these parameters, the shoulders near *ab*

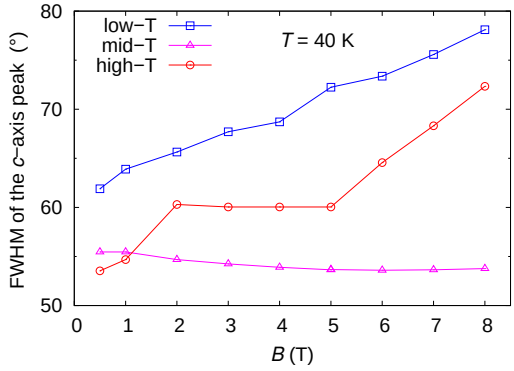

Figure 22. The FWHM values of the c peak at 40 K, calculated from the vortex path fits to the angular data. The BZO content in the samples is 5 wt.%. [**P1**]

Table 5. The length of the vortex steps λ in different sample regimes. Γ_L is proportional of the Lorentzian width of the fitted curve and m is the average number of the steps vortices take. The original data is measured at 40 K and the fitted parameter Γ_L is an average, obtained from measurements at 3 T and 5 T.

T_{dep} (°C)	Γ_L	m	λ (nm)
700 (low-T)	1.2	8	19.5
725 (mid-T)	1.0	5	32.2
775 (mid-T)	0.9	3	44.9
800 (mid-T)	0.9	3	43.6
825 (high-T)	1.1	8	21.8

peak can also be modelled. The obtained values are similar to the ones seen before [28], although the small discrepancies can be explained with the differences in the deposition conditions, like the deposition temperature.

Gamma (or Γ_L due to strong Lorentzian nature of the peaks) is related to vortex step length by [27, 28]

$$\Gamma = \frac{\sigma}{\sqrt{m}\lambda}, \tag{16}$$

where σ is the standard deviation of the mutual distances of the pinning sites, assumed as 34 nm [28], m the average number of steps that a vortex takes and in the c direction $m\lambda$ equals with he thickness of the film. The average number of steps and step lengths are shown in table 5 along with the averaged value of the fitted Γ_L into the measurements

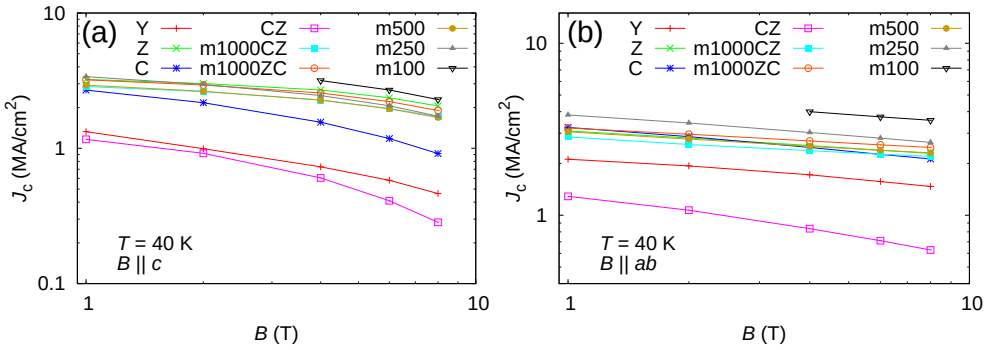

Figure 23. The magnetic field dependencies of the critical current density of the multilayer samples at 40 K as the magnetic field is parallel to YBCO c axis (a) and ab plane (b). The data is extracted from the measured angular dependencies of J_c. Due to the current limitations of the measurement system, some low-field data could not be measured. [**P5**, SI]

done at 3 T and 5 T field at 40 K. The largest step length due to smallest Γ_L is on the 775 °C sample. When there is no c peak, there are more steps which are shorter. Even though there are straight rods in the high-T samples, they are not entirely continuous and also the stacking faults disturb the vortices and no c peak is seen. As a conclusion, it can be said that the existence of the correlated defects does not necessary imply a c peak.

5.2.3 Multilayer samples

The length of the columnar defects is controlled in the multilayer samples. The defect structure gives rise to J_c, as can be seen from the $J_c(B)$ curves extracted from the resistively measured angular dependencies of J_c (figure 23). As $B||c$ axis of YBCO (figure 23 (a)), the sample m100 with the shortest columns has the highest values but otherwise the differences between the samples having columnar defects can be accounted to statistical variation. All of them have J_c values remarkably higher than those of BCO doped C, undoped Y and sample with both BZO and BCO doping, CZ. The in-field behaviour is rather similar in all samples with columnar defects, apart from m250 whose J_c deteriorates slightly faster than on other samples. However, this may be related to sample-to-sample variation because no other film behaves similarly. As $B||ab$ plane of YBCO (figure 23 (b)), the situation changes. The Z sample is not any more among the best samples, but the multilayer m100 is highest also in this direction. This suggests that

also here the continuous rods degrade the J_c in the *ab* direction more than discontinuous rods. Additionally, the pinning capability of CZ is remarkably decreased.

The exact J_c values depend on critical voltage criterion but also on the way measurements are made [19] and similar enhancements can also be obtained using surface pinning [114] or multilayer structure of undoped samples as well [115, 116]. It was seen in [115] that the longer deposition time of a multilayer structure of layers YBCO and $NdBa_2Cu_3O_{7-\delta}$[115], allowed the interfaces to relax. However, the stress due to lattice mismatch is relieved through out-of-plane edge dislocations that enhance J_c. Improvements in J_c are seen even if the film is deposited using only a YBCO target but dividing the deposition into several parts, as if depositing a multilayer structure [116]. In this thesis, differences in the strain of the BCO and BZO doped YBCO are seen. This causes the transition from one layer into another not to be smooth which could probably trigger similar kind of out-of-plane edge dislocations seen in [115, 116]. Generally, the interfacial misfit dislocations are suggested to improve the self-field J_c [17].

Additionally, because the rods in the upper layers are not at the same positions as those in the bottom layer, in the case $B||c$ axis of YBCO, there is a rather dense network of pinning centres. This is in contrast to for example Matsumoto *et al.* where nanorods grew on top of each other but no increase in J_c throughout all angles were seen. In low fields, the pinning sites are strong enough for vortices and in higher fields the BCO particles between the rods stop the vortices from moving. A vortex kink cannot slide along the rod because it would cost extra energy for the vortex to leave the dot pinning site. This is not the case if the spacer layer is undoped YBCO [59, 117] that lacks defects with pinning strength close to BZO rods. Additionally, the rod not being on top of each other, there are more pinning sites for the vortices to be pinned at high magnetic fields as well [**P3**]. However, the different alignment of the rods in [59, 117] may also affect the pinning force strength and thus direct conclusions about the pinning capability of the dot layer may not reliably be drawn.

The angular dependencies of the multilayer samples are shown at 40 K, 4 T in figure 24 (a). The relatively high field allows to see the vortex-vortex interactions and 40 K allows to see data on all angles, which was not possible a 10 K due to the current limitations of our measurement system. The samples that have long enough rods, down to m500, have a *c* peak but m250 and m100 do not exhibit that peak any more. In other words, the rod length of roughly 38 nm is not long enough for *c* peak. The disappearance of the *c* peak is similar to seen in [**P1**], but also in BSO doped YBCO multilayers [59]. However, as noted in [59], the ends of the rods act as powerful pin-

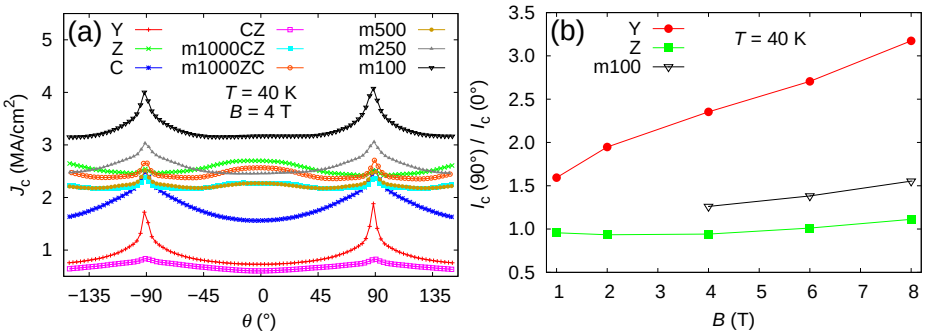

Figure 24. (a) The angular dependencies of J_c of the multilayer samples at 40 K, 4 T. (b) The ratio $I_c(90°)/I_c(0°)$ at 40 K on the multilayer samples. [**P5**]

ning centres even when the field is perpendicular to the rods. The m100 sample has the highest J_c throughout, mainly due to the same reasons that cause high J_c at $\theta = 0°$. Additionally, the short rods allow vortices to be easily pinned even if the field is far away from the direction of the rods. If a vortex jumps from one pinning site into another, there are more possibilities where it can go as compared to sample with straight and continuous rods.

At 10 K, the $J_c(\theta)$s are similar to 40 K (figure 25 (a)). Samples that have long rods, down to m1000ZC and m1000CZ, exhibit a double peak structure due to tilted and flexural rods. The tilt can be adjusted by tuning the deposition temperature [**P1**]. At 77 K (figure 25 (b)) there are no *c* peaks any more but shoulders evolve near the *ab* peak. The the m100 has still the highest J_c values throughout all angles. The rods are not efficient enough close to T_c due to thermal depinning and larger vortices. This results in more diverse paths for vortices and thus the disappearance of the *c* peak [28].

Also in this case the anisotropy of the samples was determined by calculating the ratio $I_c(90°)/I_c(0°)$. The Blatter-type scaling cannot be used, like in [76], due to the *c* axis peak and, furthermore, there are difficulties in using the Blatter-type curve on J_c [**P3**]. The ratios are shown for the Y, Z, and m100 in figure 24 (b). As in [**P1**], also here, the most continuous columns give the smallest ratio, pretty close to one at all temperatures but again this is not the same as the maximum to minimum ratio due to the *c* peak. The ratio for m100 is around 1.5, rising towards higher fields. It is also similar to low-T samples seen in figure 21 (b). The rather low ratio is partly due to the high absolute J_c of m100 as even a rather large absolute drop is seen as a small relative decrease. The undoped Y is rather similar to the high-T samples, albeit for the high-T

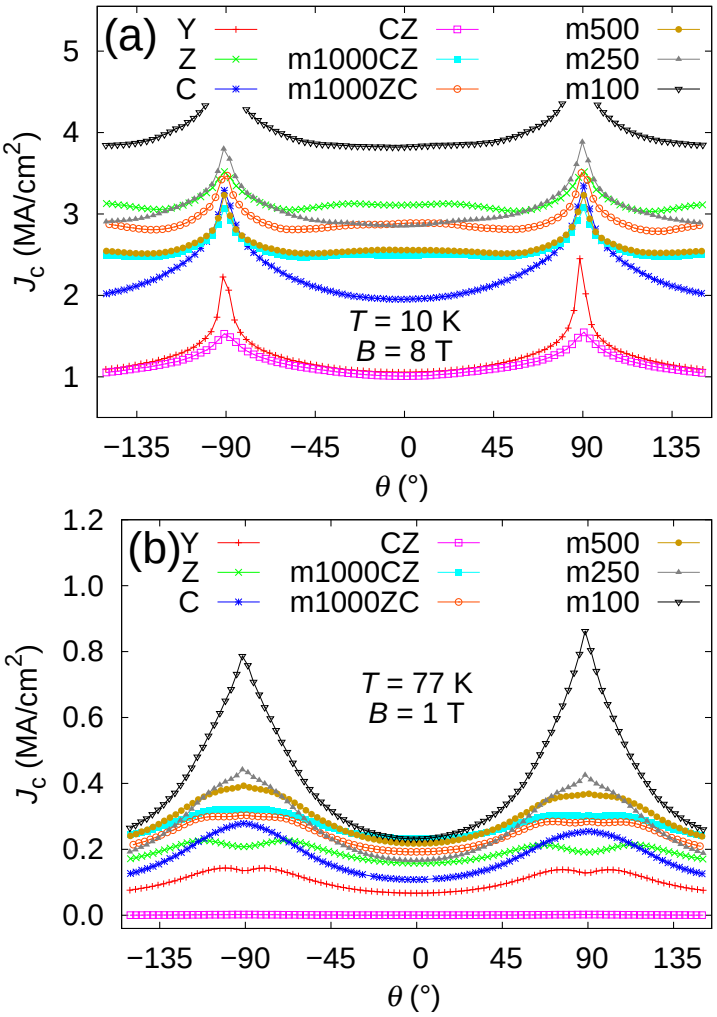

Figure 25. The angular dependencies of J_c of the multilayer samples at 10 K, 8 T (a) and 77 K, 1 T (b). Part of the data for 10 K is missing due to the limitations of the measurement system. [**P5**, SI]

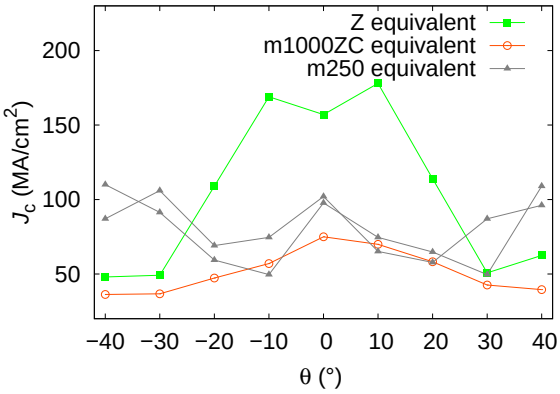

Figure 26. The modelled angular dependencies for the Z, m1000Zc and m250 equivalent samples at 0.75 T field. The m250 equivalent has been calculated using two slightly different pinning landscapes. [**P5**]

samples the ratio is even higher at high fields. As a conclusion, it can be said that the pinning site morphology affects greatly on the anisotropy of the samples, as also seen on the work of Horide *et al.* [70].

5.2.4 Simulations of multilayer samples

Using the molecular dynamics simulation presented in chapter 3 for Z, m1000ZC and m250 equivalent structures, the *c* axis peak can be reproduced. In the simulation, the peak is observed on Z and m1000Zc equivalent, but not on m250 which has four BZO and four BCO doped YBCO layers (figure 26). The schematic structure of the samples is shown in figure 12. The simulation for m250 equivalent was run twice with slightly altered pinning site positions to probe effect of randomness but nonetheless there is not enough statistics to say whether the small peak-like feature seen is a real peak. Experimentally, small peak can be a result of large amount of dislocations in undoped samples [118]. The absolute value of Z is higher than the m250 which is not the case in the experimental results. Thus, in the real samples there are other pinning mechanisms although nanoinclusions are the strongest ones [22, 103].

Figure 27 shows the steady-state behaviour of vortices at the critical current value of Z equivalent samples at different angles with respect to the rods. The rods pin the vortices up to -20° tilt, and vortices are turned parallel to the rods. However, at -40°, they act more like point pinning centres which decreases the J_c value. Additionally, the

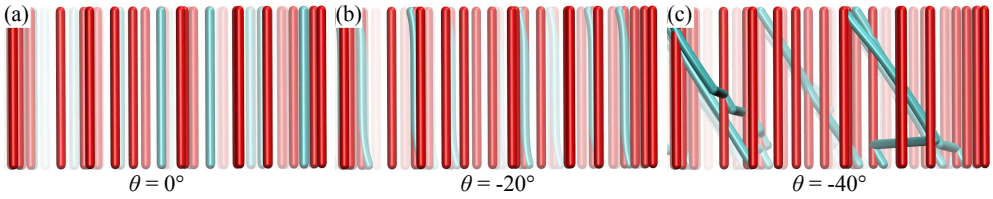

Figure 27. Vortices at the steady state with current at the critical limit in the rod sample with the angle of the magnetic field (a) 0° (b) -20° and (c) -40° with respect to the rods. The rods are red and vortices turquoise and the density of vortices corresponds to a 0.75 T field. The Lorentz force is directed out from the figure. The illustrations were made using VMD [119]. [**P5**]

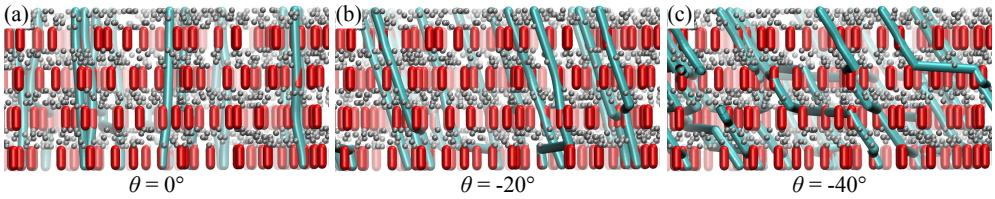

Figure 28. Vortices at the steady state with current at the critical limit in the m250 equivalent sample with angle (a) 0° (b) -20° and (c) -40° with respect to the rods. The rods are red, point pinning sites grey and vortices turquoise and the density of vortices corresponds to a 0.75 T field. The Lorentz force is directed out from the figure. [**P5**]

high current causes a high Lorentz force which in turn causes the vortices to be longer. The line tension force is not strong enough to keep vortices as short as possible.

In the m250 equivalent sample the vortices behave differently with respect to the rods as the angle of the magnetic field is changed. As B is parallel to the rods, vortices mainly follow them. In the simulation, rods are not on top of each other so that the situation better corresponds to the experimental results. This configuration along with the shortness of the rods makes them more like point pinning centres and at even 0° not all vortices go along the rods. At -20°, vortices do not follow the rods any more, but rather go along the field. The rods are less and less capable to pin the vortices and the number of the jumps that vortices take, becomes larger. This behaviour with shorter rods is also suggested by the vortex path model in [**P1**]. Additionally, although it is seen that dots improve pinning, their effect is rather small compared to the rods. However,

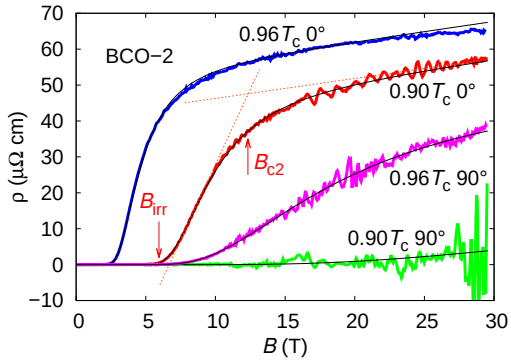

Figure 29. An example of resistivity versus magnetic field for BCO-2 at two angles at $0.96T_c$ and $0.90T_c$. The arrows indicate B_{irr} and B_{c2}, the latter being at the intersection of two dotted tangents. The solid line is a phenomenological fit into the data to ease the analysis. [**P4**]

the model may underestimate the effect of rods because it only takes into account their actual size, not the strain they create in the YBCO matrix [**P3**].

5.3 Dopant effect on intrinsic anisotropy

5.3.1 Spherical particles

The properties of YBCO are naturally anisotropic and the anisotropy is often determined by applying Blatter scaling (equation (3)) into $J_c(\theta)$ data as $J_{c0}/\varepsilon_\vartheta(\theta)$, where J_{c0} is J_c as $B||c$ axis of YBCO. In such a case, anisotropy is lowered and γ is decreased with doping [108, 120, 121] but due to the extrinsic nature of J_c it is denoted as γ_{eff}. Additionally, doping has seen to decrease the intrinsic anisotropy [74, 75] but also constant γ in doped samples has been reported [45, 76]. However, also in the reports with constant γ, an increase in B_{c2} was seen.

To find out the effect of spherical BCO particles on B_{c2} and intrinsic anisotropy, 2 wt.% and 8 wt.% BCO doped YBCO thin films (called BCO-2 and BCO-8 hereafter) were measured in pulsed magnetic fields up to 30 T. The data for the undoped reference sample was taken from [74]. The critical fields were extracted from the resistivity, ρ, versus magnetic field, B, curves, and an example is shown in figure 29. To ease the analysis, data was fitted using a phenomenological equation, a straight line multiplied by an exponent function [57, 74]. Figure 29 also shows fits to the data, along with the defined B_{c2} and B_{irr} for one curve.

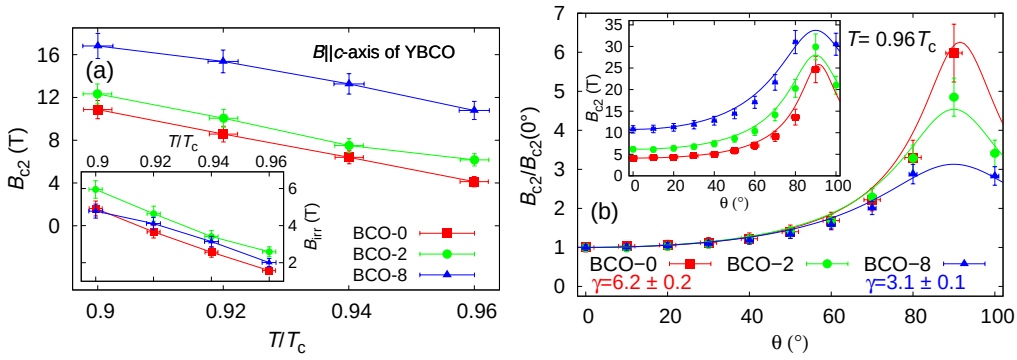

Figure 30. (a) The temperature dependence of B_{c2} at $\theta = 0°$. The inset shows the temperature dependence of B_{irr} at the same angle. (b) The angular dependencies of B_{c2} in different BCO doping levels at $0.96T_c$, scaled with the field out-of-plane value of B_{c2}. Inset shows the same data unscaled. Solid lines are Blatter scaling fits of B_{c2}. **[P4]**

The B_{c2} has a linear dependence on temperature in the measured range, from $0.90T_c$ to $0.96T_c$ (figure 30 (a)). The higher is the BCO content, the higher is B_{c2}. The errors in the figure are a sum of the errors owing to fitting of the phenomenological $\rho(B)$ equation and uncertainties in the magnetic field and temperature using the total differential with the assumption that all the errors occur at the same time. The curves in figure 30 (a) also give another way to define critical temperature. T_c can be obtained as the curves are extrapolated linearly to zero field (called as extrapolated T_c hereafter). It yields 88.3 K [74], 88.9 K and 89.0 K for BCO-0, BCO-2 and BCO-8, respectively. The values are higher than the magnetic T_cs due to the percolative current in the measurements. The measurements were done between $0.90T_c$ and at $0.96T_c$ relative to the magnetically defined T_c and thus relative to the extrapolated T_c, BCO-8 was measured at lower temperature than BCO-2. However, it is seen that the resistive and magnetic T_c of BCO doped samples correspond well to each other with almost constant shift (figure 31 (b) inset) and thus the magnetic T_c is a good proxy for resistive zero-field T_c. The inset of figure 30 (a) shows the B_{irr} values close to each other with rather linear dependence on temperature in this scale. Additionally, the values are close to the ones of BZO doped samples [58].

As can be seen in figure 30 (b), the higher is the BCO concentration, the higher is B_{c2} at all angles. Relative change is largest at $\theta = 0°$, i.e. $B||c$ axis of YBCO. The increase of B_{c2} with concentration could be due to differences in the extrapolated T_c and magnetic T_c. However, the anisotropy parameter γ has been seen to be constant roughly

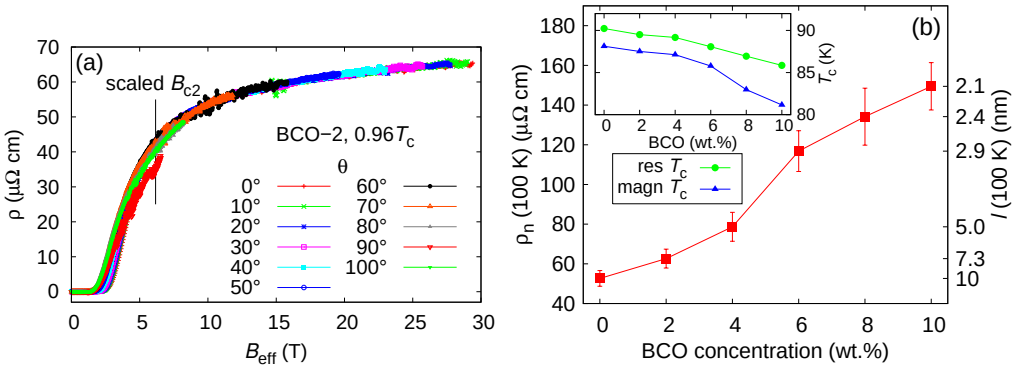

Figure 31. (a) The resistivities of BCO-2 at $0.96T_c$ at different angles against the effective magnetic field. The vertical line shows the position of B_{c2}. (b) The normal state resistivity at 100 K as a function of BCO concentration, measured for [**P3**]. The mean free paths estimated from that data are shown on the right axis. The inset shows both magnetic and resistive T_c of the same set of samples. [**P4**]

below $0.95T_c$ [45, 75] and thus small differences in the measurement temperatures are unlikely to affect that result remarkably.

Solid lines in the figure 30 (b) are fits to Blatter scaling applied into B_{c2} as $B_{c2}(\theta = 0°)/\varepsilon_\vartheta(\theta)$. Apart from the absolute value, there are no large differences in the measured B_{c2} at $0.90T_c$ and $0.96T_c$. Thus the function was fitted simultaneously for both temperatures. The maximum magnetic field pulse being 30 T, the B_{c2} values larger than that were omitted as unreliable. In practice, this means at $0.90T_c$ angles greater than 60°. With these restrictions, the function describes the data well at all angles. The fit yields γ value 6.2 for the undoped and 4.5 and 3.1 for BCO-2 and BCO-8, respectively.

To further ensure that the Blatter scaling works for the data, the resistivities were plotted against effective magnetic field as $B_{eff} = B\varepsilon_\vartheta$ (figure 31 (a)), as also done in [108, 122]. From the scaled resistivity scans of BCO-2 at $0.96T_c$, it can be seen that the curves indeed collapse into single point at B_{c2} but, around B_{irr}, there is a larger spread of the curves. The figure also shows that not all angles the 30 T pulse is not enough to reach B_{c2}. The scaling works similarly for other samples as well.

The decrease of γ is seen in both BZO [74] and BCO doped YBCO thin films. It has been suggested that this change of γ is due to scatter of electrons from the YBCO-dopant interface or due to the strain fields around the dopant [75, 123]. Similar disorder-triggered improvement of B_{c2} is also seen on Nb_3Sn [124].

The increase of B_{c2} can be explained by using the dirty-limit of superconductors. The Ginzburg-Landau theory in the dirty limit [125, 126] states that in the case of isotropic scattering the anisotropy parameter can be replaced by the diffusivity ratio which depends on the electron mean free path (mfp) of the material [127].

In the unrestricted limit, B_{c2} is related to γ and ξ as

$$\gamma = \frac{B_{c2,ab}}{B_{c2,c}} = \frac{\xi_{ab}}{\xi_c}, \tag{17}$$

where B_{c2ab} and B_{c2c} correspond to cases $B||ab$ plane and $B||c$ axis of YBCO. By using the impurity-restricted ξ (equation (1)) and the temperature dependence of ξ [128, p. 145, 148] as $\xi \propto (1 - T/T_c)^{-1/2}$, it can be calculated that at $0.90T_c$ for BCO-2 $\xi_{0,ab} =$ 4.8 nm and $\xi_{0,c} = 0.9$ nm and for BCO-8 $\xi_{0,ab} = 4.0$ nm and $\xi_{0,c} = 0.8$ nm. This yields impurity restricted mean free paths as 20 nm and 3.8 nm for BCO-2 and BCO-8, respectively.

It is also possible to estimate the mfp from the normal state resistivity values. A clear increase with rising BCO concentration can be seen in figure 31 (b), error bars originating from the uncertainties in the measured stripe dimensions. The resistivities can be converted into mfp values at 100 K (the scale on the right hand side) by assuming that the mfp of an undoped sample is equal to that of single crystal sample, 10 nm [129] and that the increase in resistivity is due to impurity scattering. As a result, dopants decrease the mfp remarkably. In practice, in thin films there are more defects, like twin boundaries [130] that further limit the mfp considerably. Thus this calculation overestimates the value of mfp. If using the mfp at $0.90T_c$ for single crystal, and assuming the same resistivity ratios, we get the mfp values of 22 nm and 7.3 nm for BCO-2 and BCO-8, respectively.

Furthermore, a simple numerical simulation, based on the uniform distribution of the BCO particles, with size distribution taken from figure 9 in chapter 4.1 yields a mfp of 31 nm and 15 nm for BCO-2 and BCO-8. All the obtained mfp values are close to the ones calculated from the B_{c2} data and impurities are clearly seen to decrease it. The mfp is also shortened by strain and other defects present in the films and their effect can be especially seen in BCO-8.

Additionally, because $\xi_c < \xi_{ab}$, a uniform restriction of mfp causes a larger change in the impurity restricted ξ_{ab}. This causes the change of the B_{c2} in the c direction to be larger than in the ab direction. The anisotropic change of B_{c2} results in the decrease of γ. The same theory can be used to explain the increase of B_{c2} in BZO [74] and $BaHfO_3$ [123] doped YBCO. In the case of large BZO particles in CSD made YBCO films [76],

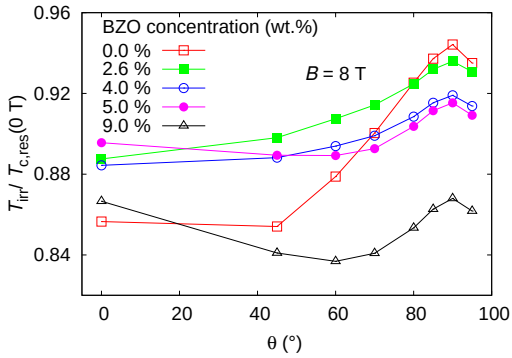

Figure 32. The irreversibility temperature of BZO doped samples scaled using the zero-field transition temperature as a function of the angle between YBCO c and magnetic field, measured at 8 T. [**P2**]

no changes were observed because the distance between particles is large and does not restrict the mfp and no change in γ is observed.

5.3.2 Columnar defects

The B_{c2} and B_{irr} of BZO doped samples were studied by resistively measuring transition temperatures at constant magnetic fields. The T_c defined from each curve corresponds to B_{c2} at that field and the temperature at which the resistance starts to rise from zero, corresponds to B_{irr}. The irreversibility temperature, T_{irr}, at certain magnetic field corresponds to B_{irr} at certain temperature. From figure 32 it can be seen that at 8 T, T_{irr} clearly depends on the BZO concentration. At $\theta = 0°$, the middle concentrations have the highest values and there is clear a c peak on samples with high BZO content. The highest concentration has a low value due to increased ΔT_c. While decreasing the field, the c peak becomes more flat and the undoped does not any more have the lowest T_{irr} value. Similar trends have been noted also in pulsed magnetic field measurements [58]. At fields 2 T and below, at $\theta = 0°$ undoped has the largest B_{irr}, which decreases with concentration. Similar B_{irr} dependence has seen in magnetic measurements of the samples under study here [131]. At $\theta = 90°$, T_{irr} decreases monotonically with increasing BZO concentration which suggests that the distraction of the rods affects also here.

The B_{c2} as a function of the reduced temperature, t, i.e. temperature scaled with the zero-field resistive T_c, does not show clear trend with the BZO concentration (figure 33 (a)). The 9 wt.% concentration degrades the properties and that decreases the B_{c2} with respect to lower BZO content. There are no significant differences between those

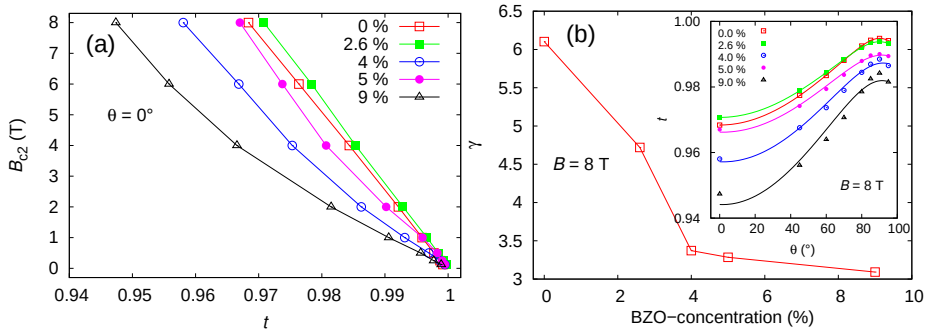

Figure 33. (a) The dependence of the upper critical field, B_{c2}, as a function of the reduced temperature, t, in samples with different BZO concentrations at $B||c$ axis of YBCO. (b) Inset: The $B_{c2}(\theta)$ and equation (18) fitted on the data. The main panel shows the evolution of γ extracted from the fits at the inset as a function of the BZO concentration. [**P2**]

samples, the small differences are likely due to the small high-T_c phase and uncertainties related to determining the B_{c2}. This is in contrast to measurements of B_{c2} in pulsed magnetic fields [74] and magnetic measurements of B_{c2} [123, 131] where changes of B_{c2} with doping were seen. This emphasizes the different nature of the measurement configuration because the samples are exactly the same as in [131] and similar to [74]. They may originate from the small probing current going in the tiny high-T_c phase that was especially compensated in [74] by using slightly higher deposition temperature.

The angular dependence of B_{c2} extracted from the measurements of $R(T)$ curves at 8 T behaves differently to B_{irr} (figure 33 (b) inset). There is no c peak and the drop of B_{c2} with rising concentration in that direction is relatively high as compared to the ab direction. Even though the B_{c2} of the undoped sample is among the highest ones, the decrease of B_{c2} does not occur monotonically with concentration but differences may also be caused by the sample-to-sample variation. However, the 9 wt.% sample has the lowest values due to lower T_c and degradation owing to high BZO concentration.

The anisotropy of the obtained B_{c2} curves was calculated by fitting a function containing the anisotropy parameter γ. The equation

$$\frac{T}{T_c}(\theta) = 1 - \frac{B_{c2}}{2B_0}\left(\frac{\sin^2(\theta)}{\gamma^2} + \cos^2(\theta)\right)^{1/2} \tag{18}$$

is combined from the Ginzburg-Landau expression for the temperature dependence of B_{c2} [128, p. 53] and Blatter scaling [16]. In the equation, B_0 is B_{c2} at 0 K. The fitted

curves are given in figure 33 b inset. The curves fit the data best with low BZO content, maybe due to the high-T_c phase in high concentration. For the undoped YBCO, the γ equals 6, similar than before [106]. The doped samples have γ between 3–3.5 which is close to the measurements in pulsed magnetic fields [74].

As a whole, this measurement setup is capable to give rather reasonable results of γ. The result is similar to BCO doped YBCO in the previous chapter and similar mechanisms can be used to explain the observed decrease. However, due to the small probing current, especially the absolute value of B_{c2} is extremely sensitive to variations in T_c.

6 Conclusions

In this thesis, YBCO thin films with BCO and BZO doping were studied. Both dopants were seen to improve pinning, but as deposited on STO using PLD, they behave very differently in the YBCO matrix. According to the TEM images, BCO in YBCO matrix creates spherical particles that are randomly distributed but also some clusterisation along the *ab* planes of YBCO was seen. The diameter of the particles is couple of nanometres and it is increases with the dopant concentration. Because of the shape of the particles, dopant has a large interface area with YBCO and thus creates remarkable strain in the YBCO matrix and increases the *c* lattice parameters.

The BCO dopant also decreases T_c some kelvins and broadens the transition. The point-like particles offer some improvement in $J_c(B)$ although the self-field J_c decreases with doping, partly due to degradation of the crystal quality with doping. In the angular dependence of the critical current, only a slight broadening of the *ab* peak can be seen. Because the particles are random, no *c* peak, typical to correlated columnar defects, was seen. BCO was, however, seen to clearly improve the B_{c2} and decrease the intrinsic anisotropy parameter γ. Defects shorten the electron mean free path and thus decrease the ξ, especially in the *ab* direction. This leads to a uneven changes in B_{c2}, and finally changes in γ. Similar improvement of B_{c2} has been before seen with BZO doping.

In contrast to BCO, BZO creates columnar defects that are parallel to YBCO *c* axis. The splay of the rods can be controlled by varying the deposition temperature in the PLD process. Too low temperature creates splayed and short rods whereas too high temperature produces straight but discontinuous rods. Unlike for BCO, the rod diameter does not depend on concentration but with higher concentration, more rods are obtained. Due to smaller lattice mismatch and smaller interface area compared to BCO, BZO causes much less strain in the YBCO matrix.

Similarly to BCO, BZO causes a drop in the transition temperature but does not broaden the transition significantly. The in-field values of J_c are greatly improved, especially in the *c* direction, as compared to undoped sample. If the rods are straight and continuous, a *c* peak can be seen in the angular dependence of the critical current, having also greatly decreased effective anisotropy. If the rods are non-continuous either with or without splay, there is not any more a *c* peak. According to the vortex path model, if vortex step length along the (columnar) pinning site is shorter than the standard deviation of the sideways steps, no peak can be seen.

The dopants were also combined in multilayer films with layers having either BCO or BZO doped YBCO. The thicknesses of the films was kept constant and the number of

layers was varied. The most isotropic film with respect to $J_c(\theta)$ is still the BZO doped monolayer but the multilayer structure causes the J_c to increase further due to strain relief at the interface of differently doped YBCO layers. The multilayer structures affect also the angular dependence significantly. If the straight BZO rods are short enough due to high number of layers, i.e. thin individual layers, no c peak was seen in $J_c(\theta)$. The situation is similar to the BZO rods controlled by the deposition temperature. The angular dependence of the samples was also reproduced in the developed molecular dynamics model capable of anisotropy scaling.

As a whole, flux pinning in YBCO is a complex topic and thus for each application the YBCO structures should be separately optimized according to operation temperature, field and current requirements. The samples in this thesis were deposited on single crystal substrates and additional optimization needs to be done for technical substrates but knowledge on the behaviour of the dopants on single crystals can be utilized in modification of the desired flux pinning structure in YBCO films for technical substrates. In addition, the model developed could be used as an aid in that work to make YBCO wires even more widely spread.

References

[1] S. Nishijima *et al.*, Supercond. Sci. Technol. **26**, 113001 (2013).

[2] B. G. Marchionini, Y. Yamada, L. Martini, and H. Ohsaki, IEEE Trans. Appl. Supercond. **27**, 0500907 (2017).

[3] P. Waide and C. U. Brunner, *Energy-Efficiency Policy Opportunities for Electric Motor-Driven Systems* (OECD Publishing, 2011).

[4] S. Anders *et al.*, Physica C **470**, 2079 (2010).

[5] X. Obradors and T. Puig, Supercond. Sci. Technol. **27**, 0440031 (2014).

[6] Y. B. Kim, C. F. Hempstead, and A. R. Strnad, Phys. Rev. Lett. **9**, 306 (1962).

[7] B. Batlogg, Physics today **44**, 44 (1991).

[8] D. Rybicki *et al.*, Nat. comm. **7**, 11413 (2016).

[9] J. G. Bednorz and K. A. Müller, Z. Phys. B **64**, 189 (1986).

[10] Y. Kamihara *et al.*, J. Am. Chem. Soc. **128**, 10012 (2006).

[11] A. P. Drozdov *et al.*, Nature **525**, 73 (2015).

[12] C. Kittel, *Introduction to Solid State Physics, 8th ed.* (John Wiley & Sons, Inc, 2005).

[13] B. I. Bleaney and B. Bleaney, *Electricity and Magnetism* (Oxford Science Publications, 1976).

[14] J. Bardeen, L. N. Cooper, and J. R. Schrieffer, Phys. Rev. **108**, 1175 (1957).

[15] V. L. Ginzburg and L. D. Landau, Zh. Eksp. Teor. Fiz. **20**, 1064 (1950).

[16] G. Blatter *et al.*, Reviews of Modern Physics **66**, 1125 (1994).

[17] S. R. Foltyn *et al.*, Nat. Mater. **6**, 631 (2007).

[18] H. P. Wiesinger, F. M. Sauerzopf, and H. W. Weber, Physica C **203**, 121 (1992).

[19] A. V. Pan, I. A. Golovchansky, and S. A. Fedoseev, EPL **103**, 17006 (2013).

[20] C. Cai *et al.*, Phys. Rev. B **69**, 104531 (2004).

[21] M. Peurla *et al.*, Supercond. Sci. Technol. **19**, 767 (2006).

[22] P. Paturi, M. Malmivirta, H. Palonen, and H. Huhtinen, IEEE Trans. Appl. Supercond. **26**, 8000705 (2016).

[23] H. Palonen, J. Jäykkä, and P. Paturi, Phys. Rev. B **85**, 024510 (2012).

[24] L. Krusin-Elbaum *et al.*, Phys. Rev. B **39**, 2936 (1989).

[25] U. Welp *et al.*, Phys. Rev. Lett. **62**, 1908 (1989).

[26] N. J. Long, N. M. Strickland, and E. F. Talantsev, IEEE Trans. Appl. Supercond. **17**, 3684 (2007).

[27] N. J. Long, Supercond. Sci. Technol. **21**, 025007 (2008).

[28] P. Paturi, Supercond. Sci. Technol. **23**, 025030 (2010).

[29] S. Wimbush and N. Long, New J. Phys. **14**, 083017 (2012).

[30] R. Knibbe *et al.*, Supercond. Sci. Technol. **29**, 065006 (2016).

[31] M. K. Wu *et al.*, Phys. Rev. Lett. **58**, 908 (1987).

[32] D. Larbalestier, A. Gurevich, D. M. Feldmann, and A. Polyanskii, Nature **414**, 368 (2001).

[33] M. A. Beno *et al.*, Appl. Phys. Lett. **51**, 57 (1987).

[34] K. Momma and F. Izumi, Journal of Applied Crystallography **44**, 1272 (2011).

[35] R. Liang, D. A. Bonn, and W. N. Hardy, Phys. Rev. B **73**, 180505 (2006).

[36] J. D. Jorgensen *et al.*, Phys. Rev. B **36**, 3608 (1987).

[37] E. D. Specht *et al.*, Phys. Rev. B **37**, 7426 (1988).

[38] B. Oh *et al.*, Phys. Rev. B **37**, 7861 (1988).

[39] D. R. Harshman *et al.*, Phys. Rev. B **36**, 2386 (1987).

[40] B. Dam *et al.*, Nature **399**, 439 (1999).

[41] S. K. Streiffer, E. M. Zielinski, B. M. Lairson, and J. C. Bravman, Appl. Phys. Lett. **58**, 2171 (1991).

[42] P. Paturi, M. Peurla, K. Nilsson, and J. Raittila, Supercond. Sci. Technol. **17**, 564 (2004).

[43] D. T. Verebelyi *et al.*, Appl. Phys. Lett. **78**, 2031 (2001).

[44] J. Wang *et al.*, Appl. Phys. Lett. **92**, 082507 (2008).

[45] A. Xu, J. Jaroszynski, F. Kametani, and D. Larbalestier, Appl. Phys. Lett. **106**, 052603 (2015).

[46] D. Xu, Y. Wang, L. Liu, and Y. Li, Thin Solid Films **529**, 10 (2013).

[47] H. R. Wenk, A. Chakhmovradian, and S. Foltyn, Mater. Sci. Eng. A **205**, 9 (1996).

[48] S. Sievers, F. Mattheis, H. U. Krebs, and H. C. Freyhardt, J. Appl. Phys. **78**, 5545 (1995).

[49] G. Blatter, V. B. Geshkenbein, and J. A. G. Koopmann, Phys. Rev. Lett. **92**, 067009 (2004).

[50] I. Levin *et al.*, Journal of Solid State Chemistry **175**, 170 (2003).

[51] A. Erb, E. Walker, and R. Flükiger, Physica C **245**, 245 (1995).

[52] J. L. MacManus-Driscoll *et al.*, Nat. Mater. **3**, 439 (2004).

[53] A. Goyal *et al.*, Supercond. Sci. Technol. **18**, 1533 (2005).

[54] H. Yamada *et al.*, Supercond. Sci. Technol. **17**, S25 (2004).

[55] J. Z. Wu *et al.*, Supercond. Sci. Technol. **27**, 044010 (2014).

[56] K. Traito *et al.*, Phys. Rev. B **73**, 224522 (2006).

[57] M. Peurla *et al.*, Phys. Rev. B **75**, 184524 (2007).

[58] H. Huhtinen *et al.*, J. Appl. Phys. **107**, 053906 (2010).

[59] K. Matsumoto *et al.*, J. Appl. Phys. **116**, 163903 (2014).

[60] C. V. Varanasi *et al.*, Supercond. Sci. Technol. **19**, L37 (2006).

[61] C. V. Varanasi *et al.*, J. Appl. Phys. **102**, 063909 (2007).

[62] H. Tobita *et al.*, Supercond. Sci. Technol. **25**, 062002 (2012).

[63] D. M. Feldmann *et al.*, Supercond. Sci. Technol. **23**, 095004 (2010).

[64] L. Opherden *et al.*, Sci. Rep. **6**, 21188 (2016).

[65] K. S. Knight and N. Bonanos, Materials Research Bulletin **30**, 347 (1995).

[66] F. Genet, S. Loridant, C. Ritter, and G. Lucazeau, J. Phys. Chem. Solids **60**, 2009 (1999).

[67] M. Irjala *et al.*, IEEE Trans. Appl. Supercond. **21**, 2762 (2011).

[68] P. Mele *et al.*, Supercond. Sci. Technol. **20**, 616 (2007).

[69] B. Maiorov *et al.*, Nat. Mater. **8**, 398 (2009).

[70] T. Horide *et al.*, Supercond. Sci. Technol. **26**, 075019 (2013).

[71] M. Irjala *et al.*, Journal of Physics: Conference Series **153**, 012014 (2009).

[72] W. Schindler *et al.*, Physica C **169**, 117 (1990).

[73] J. Ye and K. Nakamura, Phys. Rev. B **48**, 7554 (1993).

[74] H. Palonen, H. Huhtinen, M. A. Shakhov, and P. Paturi, Supercond. Sci. Technol. **26**, 045003 (2013).

[75] M. Miura *et al.*, Appl. Phys. Lett. **96**, 072506 (2010).

[76] A. Llordés *et al.*, Nat. Mater. **11**, 329 (2012).

[77] B. Dam *et al.*, Physica C **261**, 1 (1996).

[78] F. J. Baca *et al.*, Adv. Funct. Mater. **23**, 4826 (2013).

[79] Q. Xie, A. Madhukar, P. Chen, and N. P. Kobayashi, Phys. Rev. Lett. **75**, 2542 (1995).

[80] J. J. Shi and J. Z. Wu, Philosophical Magazine **92**, 2911 (2012).

[81] T. Puig *et al.*, Supercond. Sci. Technol. **21**, 034008 (2008).

[82] J. Gutiérrez *et al.*, Nat. Mater. **6**, 367 (2007).

[83] D. B. Chrisey and G. K. Hubler, *Pulsed Laser Deposition of Thin Films* (John Wiley Sons Inc., 1994).

[84] B. Dam, J. M. Huijbregtse, and J. H. Rector, Phys. Rev. B **65**, 064528 (2002).

[85] D. M. Feldmann *et al.*, Appl. Phys. Lett. **91**, 162501 (2007).

[86] Y. Ichino and Y. Yoshida, IEEE Trans. Appl. Supercond. **27**, 7500304 (2017).

[87] V. Galluzzi *et al.*, Physica C **470**, S142 (2010).

[88] M. Malmivirta *et al.*, J. Low Temp. Phys. **186**, 74 (2017).

[89] A. Gauzzi and D. Pavuna, Appl. Phys. Lett. **66**, 1836 (1995).

[90] E. Montoya *et al.*, Microscopy Research and Technique **70**, 1060 (2007).

[91] J. H. Durrell, D. M. Feldmann, and C. Cantoni, Appl. Phys. Lett. **91**, 182506 (2007).

[92] Y. Ando *et al.*, Phys. Rev. B **60**, 12475 (1999).

[93] H. Assi *et al.*, Molecular Simulation **42**, 1401 (2016).

[94] E. H. Brandt, Phys. Rev. B **34**, 6514 (1986).

[95] V. Pan *et al.*, Phys. Rev. B **73**, 054508 (2006).

[96] J. Bardeen and M. J. Stephen, Phys. Rev. **140**, A1197 (1965).

[97] T. Sekitani *et al.*, Phys B **346-347**, 319 (2004).

[98] H. Huhtinen, M. Irjala, P. Paturi, and M. Falter, IEEE Trans. Appl. Supercond. **21**, 2753 (2010).

[99] M. Sieger *et al.*, IEEE Trans. Appl. Supercond. **25**, 6602604 (2015).

[100] H. Huhtinen, K. Schlesier, and P. Paturi, Supercond. Sci. Technol. **22**, 075019 (2009).

[101] A. Augieri *et al.*, IEEE Trans. Appl. Supercond. **19**, 3399 (2009).

[102] T. Ozaki *et al.*, J. Appl. Phys. **108**, 093905 (2010).

[103] K. Matsumoto and P. Mele, Supercond. Sci. Technol. **23**, 014001 (2010).

[104] H. Huhtinen *et al.*, J. Phys. Conf. Ser. **507**, 012020 (2014).

[105] W. K. Kwok *et al.*, Phys. Rev. Lett. **67**, 390 (1991).

[106] L. Civale *et al.*, Appl. Phys. Lett. **84**, 2121 (2004).

[107] A. Palau *et al.*, IEEE Trans. Appl. Supercond. **21**, 3243 (2011).

[108] P. Paturi, M. Irjala, and H. Huhtinen, J. Appl. Phys. **103**, 123907 (2008).

[109] P. Paturi, M. Irjala, H. Huhtinen, and A. B. Abrahamsen, J. Appl. Phys. **105**, 023904 (2009).

[110] X. Wang *et al.*, J. Appl. Phys. **108**, 113911 (2010).

[111] H. Huhtinen *et al.*, IEEE Trans. Appl. Supercond. **17**, 3620 (2007).

[112] P. Paturi, M. Irjala, A. B. Abrahamsen, and H. Huhtinen, IEEE Trans. Appl. Supercond. **19**, 3431 (2009).

[113] V. F. Solovyov *et al.*, Supercond. Sci. Technol. **20**, L20 (2007).

[114] V. A. Khokhlov *et al.*, Supercond. Sci. Technol. **17**, S520 (2004).

[115] A. V. Pan, S. V. Pysarenko, and S. X. Dou, Appl. Phys. Lett. **88**, 232506 (2006).

[116] A. V. Pan *et al.*, IEEE Trans. Appl. Supercond. **17**, 3585 (2007).

[117] T. Horide *et al.*, Supercond. Sci. Technol. **29**, 105010 (2016).

[118] J. Gutiérrez, T. Puig, and X. Obradors, Appl. Phys. Lett. **90**, 162514 (2007).

[119] W. Humphrey, A. Dalke, and K. Schulten, J. Molec. Graphics **14**, 33 (1996).

[120] J. R. Clem, Phys. Rev. **153**, 449 (1967).

[121] P. W. Anderson, J. Phys. Chem. Solids **11**, 26 (1959).

[122] S. Sarti *et al.*, Phys. Rev. B **55**, R6133 (1997).

[123] T. Matsushita *et al.*, Supercond. Sci. Technol. **25**, 125003 (2012).

[124] L. D. Cooley, Y F. Hu, and A. R. Moodenbaugh, Appl. Phys. Lett. **88**, (142506).

[125] A. A. Golubov and A. E. Koshelev, Phys. Rev. B **68**, 104503 (2003).

[126] A. Gurevich, Phys. Rev. B **67**, 184515 (2003).

[127] Heon-Jung Kim *et al.*, Phys. Rev. B **73**, 064520 (2006).

[128] C. P. Poole Jr., H. A. Farach, R. J. Creswick, and R. Prozorov, *Superconductivity, Second Edition* (Academic Press, 2007).

[129] K. Krishana, J. M. Harris, and N. P. Ong, Phys. Rev. Lett. **75**, 3529 (1995).

[130] T. Jacobs *et al.*, IEEE Trans. Appl. Supercond. **7**, 1917 (1997).

[131] P. Paturi, M. Malmivirta, H. Palonen, and H. Huhtinen, J. Phys. Conf. Ser. **507**, 012040 (2014).

Annales Universitatis Turkuensis

Turun yliopisto
University of Turku

Painosalama Oy, Turku, Finland 2017

ISBN 978-951-29-7011-7 (PRINT)
ISBN 978-951-29-7012-4 (PDF)
ISSN 0082-7002 (PRINT) | ISSN 2343-3175 (PDF)